DESIGN AND DEVELOPMENT OF NON-RIGID DIAGNOSTIC AND INTERVENTIONAL MEDICAL DEVICES

by

AUSTIN JAMES TAYLOR

(Under the Direction of Zion Tsz Ho Tse)

ABSTRACT

A medical device is any apparatus, appliance, software, or material intended to be used to assist clinicians in diagnosing medical conditions, performing surgical operations, or delivering rehabilitation services. The main goal in designing new medical devices is to create more precise and less invasive methods. The advancement of medical devices has led to many commercialized robotic systems for many applications such as surgical operations, planning and simulation, minimal damage precise positioning, minimally invasive diagnosis and detection, and new types of surgery treatments.

Conventional medical devices are made of rigid materials that limit their ability to elastically deform and adapt their shape to external constraints and obstacles. These rigid devices are not ideal for many medical applications since they have the potential to damage human tissue with minimal unintentional contact. In contrast to conventional rigid devices, non-rigid devices contain little or no rigid material and are instead primarily composed of fluids, gels, soft polymers, and other easily deformable matter. Additionally, non-rigid devices can be derived from the implementation of origami

techniques to form complex three-dimensional structures which can be optimized for working within space constrained environments.

The work described in this dissertation aims to advance the field of medical devices through the design and development of novel non-rigid diagnostic and interventional medical devices. Through the examination of material properties of a composition of soft plastic, human fatty tissue was imitated to produce an abdominal biopsy phantom for training medical practitioners in CT-guided intervention. Diagnostic devices were developed using origami techniques for creating joints actuated by shape memory alloy and by 3D printing modular soft robotic pneumatic actuators. Origami was also used for developing a foldable structure for housing MRI receiver coils for use in interventional intracardiac catheterization to improve medical imaging capabilities during ablation of abnormal heart tissue in patients with atrial fibrillation.

INDEX WORDS: Origami, minimally invasive, shape memory alloy, soft robotic, magnetic resonance imaging, computed tomography

DESIGN AND DEVELOPMENT OF NON-RIGID DIAGNOSTIC AND INTERVENTIONAL MEDICAL DEVICES

by

AUSTIN JAMES TAYLOR

BS, University of Alabama, 2015

A Dissertation Submitted to the Graduate Faculty of The University of Georgia in Partial Fulfillment of the Requirements for the Degree

DOCTOR OF PHILOSOPHY

ATHENS, GEORGIA

2019

© 2019

Austin James Taylor

All Rights Reserved

DESIGN AND DEVELOPMENT OF NON-RIGID DIAGNOSTIC AND INTERVENTIONAL MEDICAL DEVICES

by

AUSTIN JAMES TAYLOR

Major Professor:	Zion Tsz Ho Tse
Committee:	Mark Haidekker
	Tianming Liu
	WenZhan Song

Electronic Version Approved:

Suzanne Barbour
Dean of the Graduate School
The University of Georgia
May 2019

ACKNOWLEDGEMENTS

There are many people I must thank for contributing to the four wonderful years of my experience as a PhD student.

First, I must thank my advisor Dr. Zion Tsz Ho Tse who, through more than 2,000 emails and many meetings over four years, molded and chiseled me from an eager but mostly confused student to a competent researcher. Zion's passion, ambition, and enthusiasm for research are infectious. When I came up with an ambitious project goal, he pushed me to work on the next step. When I produced terrible paper drafts, he patiently provided support and guidance. I am very grateful to Zion for teaching me not just about developing new technologies or the art of communicating ideas, but for teaching me how to think.

I would also like to express my gratitude towards my past and present lab-mates and friends in the Medical Robotics Lab who made my experience at UGA so pleasant: Rui Li, Brian Boland, Zhuo Zhao, Julian Moore, Kevin Wu, Alex Squires, Stan Gregory, Yabiao Guo, Rudy Montayre, and Tony Fam.

Finally, I would like to thank, most of all, my family. I was tremendously blessed to be raised by two of the most loving, caring, dependable parents, who have always provided for me and encouraged me to pursue my passions. A big thank you to my sister, Abby, who always inspires me through her compassion and creativity. Lastly, I would like to give my utmost love and appreciation to my wife, Caroline, for being my rock that

I can always count on to comfort me when times are rough, and to rejoice with me when times are good.

TABLE OF CONTENTS

Page

LIST OF TABLES

Page

LIST OF FIGURES

Page

CHAPTER 1

INTRODUCTION

Minimally Invasive Surgery

Surgical procedures are typically classified based on their level of invasiveness, of which there are three main categories: invasive procedures also known as open surgery, minimally invasive surgery, and non-invasive procedures. Minimally invasive surgeries encompass surgical techniques that minimize the size of incisions needed and so lessen wound healing time, associated pain, and risk of infection [1]. However, it is also well documented that minimally invasive surgery introduces an array of difficulties to the operating room due to the highly limited workspace, specialized tools requiring supplementary training, and significantly reduced visual and haptic information. Despite these drawbacks, minimally invasive surgery has seen continued growth and adoption rates [2, 3]. A major contributing factor in this continued adoption is the corresponding development of medical devices intended for use in minimally invasive surgery.

The two main types of minimally invasive surgery are robotic surgery and non-robotic minimally invasive surgery, also known as endoscopy. Endoscopy is a procedure that allows a physician to view the inside of a patient's body using an endoscope. Most endoscopes are thin tubes with a powerful light and tiny camera at the distal end. There are many types of endoscopes that vary in length and flexibility depending on the part of the body intended for use. Typically, an endoscope has a channel through which the physician inserts tools to collect tissue or provide treatment. These tools include biopsy

forceps, catheters, cytology brushes, suture removal forceps, and many others which can be used to diagnose a disease or to deliver treatments such as laparoscopic surgery, laser therapy, or microwave ablation. A current trend for devices being developed for use with minimally invasive surgery is to further increase the scope of applications with the design of highly function-specific devices that can be combined with medical imaging technology.

Image-Guided Therapy

Imaging has become essential not only for the detection and monitoring of disease but also for improving the outcome of therapy. Image-guided therapy helps to improve the efficacy and reduce the morbidity of minimally invasive procedures by providing intra-operative image based anatomic and physiologic information in real-time [4]. While traditional open surgery is based on hand-eye coordination, image-guided therapy advances this concept by enhancing what the eye can see with multimodal imaging, and what the hand can do with robotic and therapeutic devices. In image-guided therapy, pre-operative and real-time intra-operative imaging information is displayed, and the technologies for imaging, navigation, and therapy are all integrated with complex therapy delivery systems to transform invasive procedures into minimally invasive ones.

Outline of Dissertation

This dissertation aims to present the design and testing of several non-rigid devices developed for image-guided diagnostic and interventional therapies. These devices build in complexity throughout the following chapters, beginning with an origami lesion targeting device, and culminating in a soft robotic pneumatic actuator. The design process and the experimental validation of each device is discussed. The core focus of

this dissertation is to develop novel non-rigid medical devices which ultimately increase the efficacy of image-guided minimally invasive procedures.

References

[1] V. Velanovich, "Laparoscopic vs open surgery," Surgical endoscopy, vol. 14, no. 1, pp. 16-21, 2000.

[2] C. Tsui, R. Klein, and M. Garabrant, "Minimally invasive surgery: national trends in adoption and future directions for hospital strategy," Surgical endoscopy, vol. 27, no. 7, pp. 2253-2257, 2013.

[3] M. J. Mack, "Minimally invasive and robotic surgery," Jama, vol. 285, no. 5, pp. 568-572, 2001.

[4] K. Cleary and T. M. Peters, "Image-guided interventions: technology review and clinical applications," Annual review of biomedical engineering, vol. 12, pp. 119-142, 2010.

CHAPTER 2

ORIGAMI LESION TARGETING DEVICE FOR CT-GUIDED INTERVENTIONS

Image-Guided Interventions

Image-guided percutaneous biopsy has become an essential practice in modern medical care. It has been shown to be an effective, safe and reliable technique [1-4] to puncture lesions or provide access for drainages. Nevertheless, various complications still arise, including hemorrhaging, hematomas, and injury to surrounding anatomical structures [5-10]. The risk of complications may be amplified if the lesion location is difficult to reach or if patient positioning is suboptimal.

Traditionally, CT-guided procedures are performed using the freehand technique. This can be time consuming, especially if the target is small or difficult to reach. In these scenarios, numerous needle insertions and CT scans may be required, thus increasing time, risk, needle manipulations, tissue damage and radiation dosage. The development of guidance, navigation, and robotic systems has dramatically improved the safety and efficacy of image-guided interventional procedures. Various laser guidance systems [11-13] have aimed to improve the puncture accuracy, but these systems require the needle to stay axially aligned with the laser beam throughout the insertion and do not provide physical support to hold the needle in place. Other guidance systems have aimed to address these issues but are only able to accommodate a single needle [14-16]. Most currently used navigation systems use electromagnetic [17-27] or optical tracking systems [28-31]. Robotic positioning and guidance platforms such as the AcuBot, B-Rob, INNOMOTION,

the Mitsubishi RV-E2 lung biopsy robot, the KUKA LWR robot, the ROBIO EX, and the iSYS1 robot system provide accurate and stable needle guidance [31-40], and are especially useful in the case of limited space at the skin entry site or a difficult angulated access. The main drawbacks in computer navigated and robotic interventions include high costs for the development of such systems, complex operation of the devices, and increased operation time due to additional procedures including system set-up, instrument calibration, registration, and verification of accuracy. Thus, familiarity with these systems is important for routine and fast use. For the application of most computer navigated and robotic systems, an additional person (technician) is helpful, and the costs for the purchase of the system (approximately 100 – 300,000 $) and the additional personnel are often unaffordable for smaller hospitals.

This chapter presents a disposable origami lesion targeting device that provides a cost-effective method for holding and guiding a biopsy needle to a target location during CT guided interventions. The device removes the need for additional navigation software and patient registration. The proposed solution was evaluated using an abdominal phantom, and results of the device workspace and the lesion targeting accuracy are presented.

Design of an Origami Needle Guide

Foldable Strucutre for Needle Support

The design of the origami lesion targeting device originated from specifications suggested by surgeons and MRI interventional radiologists. Suggestions included:

- Disposable or able to be sterilized for future use
- Attached securely to patient
- Allow for in-plane or out of plane needle insertions

- Support insertion of multiple needles
- The device should not require additional software

A template-based guidance system was determined to be the most effective way to satisfy the suggested design specifications. The origami lesion targeting device (Fig. 2.1a) was constructed by laser cutting an origami folding pattern (Fig. 2.1b) from solid bleached sulphate, a virgin fiber grade of paperboard. The thickness of the paperboard can be adjusted to ensure no bending of the plane occurs upon needle insertion. An RCA grid (Fig. 2.1c) was applied to the surface of the paperboard and given time to dry before the board was turned over and another RCA grid was applied. Once both RCA grids were dry, the device was folded into its final form. Double sided mounting tape was applied to the bottom of the device to provide an effective method for mounting the device securely to the patient.

The folding pattern was designed with computer-aided design (CAD) software, AutoCAD, and cut with a Full Spectrum laser cutter. The folding pattern design consisted of five panels which fold to form a 50 mm x 100 mm x 100 mm rectangular prism with one side left open to serve as a viewing window. The dimensions can be modified to accommodate the intended application. The folded panels were held in place with eight tabs which fit snuggly into designated slots.

(a) Dimensions of the folded origami needle guide

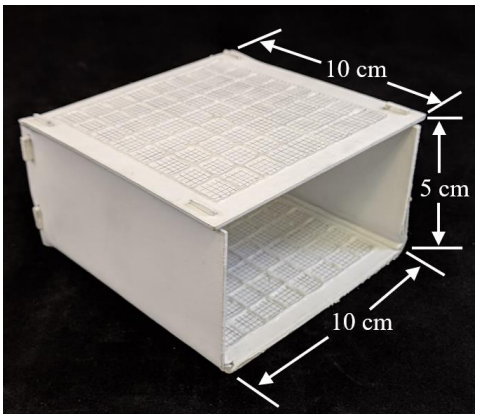

(b) Device folding pattern. Solid black lines represent cut lines and dashed red lines represent fold lines

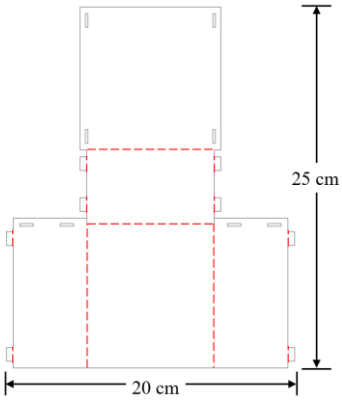

(c) Application of RCA mixture in a grid pattern.

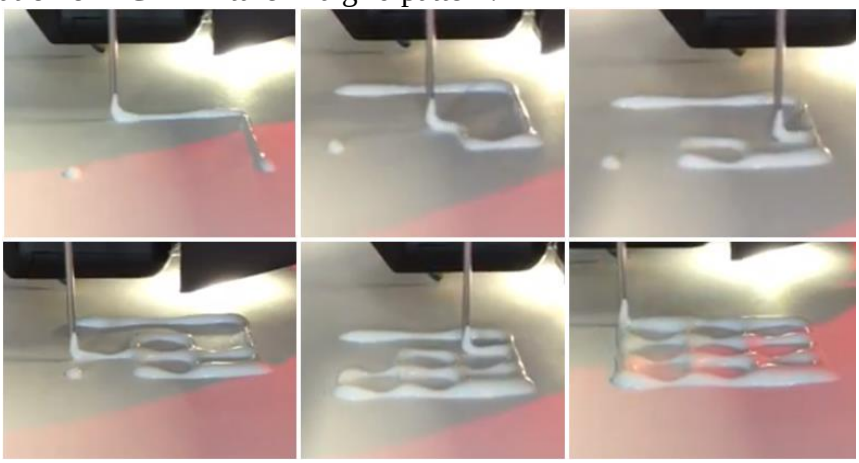

Figure 2.1. Design of an origami needle guide.

Radiocontrast Agent Mixture

The RCA mixture was developed with three major design criteria in mind. The first and most important goal was for the mixture to be bright enough to show up in a CT scan. Secondly, the mixture needed to be applied to a surface as a liquid and be able to dry into a solid. Lastly, the RCA mixture was designed to have a viscosity which would allow it to flow through a 1 mm orifice for extrusion via a syringe in a controlled manner. The resulting mixture was 80% Elmer's glue, 10% water, and 10% barium sulfate

measured by mass. Barium sulfate, Hi-LR from HiMedia Laboratiories was chosen as the radiocontrast agent due to its exceptional radiopacity [41].

Application of Radiocontrast Agent

The RCA mixture grid was applied onto the surface of the device by ejecting the mixture from a syringe with a 1 mm blunt-tipped needle. The lines of the RCA grid were applied in 1 cm increments, and additional gridlines spaced 2 mm apart were raster engraved into the top surface of the top and bottom layers to provide an effective means of measuring needle insertion locations.

Lesion Targeting Equations

Fig. 2.2 depicts a 2D schematic diagram of a needle trajectory through the device to a target lesion. From the schematic, several equations can be derived to determine the proper coordinates (x_1, y_1, x_2, y_2) in the top and bottom layers of the device through which to insert the needle to hit the target lesion. Table 2.1 defines the variables used in the targeting equations. From a CT scan, the physician can determine the desired insertion angle θ and the approximate width, length, and depth (T_x, T_y, T_z) the target is from the origin of the device. Given the target depth T_z, the vertical distance from the target layer to the bottom layer z_2 can be found by

$$z_2 = T_z - z_1 \tag{1}$$

Knowing the insertion angle, the horizontal distance from the second insertion location to the target x_b can be found by

$$x_b = \frac{z_2}{\tan\theta} \tag{2}$$

The target width T_x is the sum of the horizontal distance from the origin to the insertion location on the bottom layer x_2 and the horizontal distance from the bottom layer insertion location to the target x_b, so x_2 can be found by

$$x_2 = T_x - x_b \tag{3}$$

The horizontal distance from the origin to the top layer insertion location can be found in a similar manner by

$$x_a = \frac{z_1}{\tan\theta} \tag{4}$$

$$x_1 = x_a - x_2 \tag{5}$$

The insertion coordinates y_1 and y_2 can be found using the same equations, replacing x with y and T_x with T_y. The insertion depth can be found by

$$d = \sqrt{(x_a + x_b)^2 + (z_1 + z_2)^2} \tag{6}$$

Table 2.1 Variables in Needle Insertion Location Equations (1) – (6)

Variable	**Description**
T	Target point; $T = (T_x, T_y, T_z)$
O	Origin of device
θ	Insertion angle
x_1, x_2	Horizontal distance from origin to insertion locations
z_1, z_2	Vertical distance from top layer to bottom layer, vertical distance from bottom layer to target
x_a, x_b	Horizontal distance from top layer insertion location to bottom layer insertion location, horizontal distance from bottom layer insertion location to target
d	Needle insertion depth

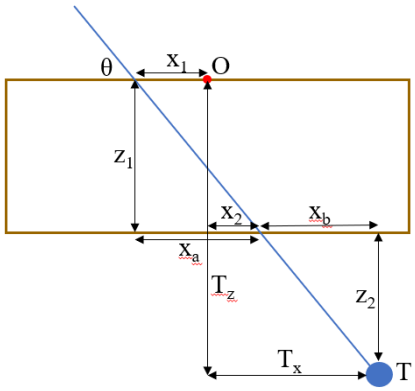

Figure 2.2. Schematic diagram of a needle insertion trajectory.

System Workflow

The workflow of a typical procedure using the device is described below.

1. Perform a diagnostic CT or ultrasound scan of the target area to locate the target lesion to determine positioning of the patient and the approximate skin entry point or region.
2. Place the needle guide on the patient and perform another CT scan to visualize the location of the target lesion with respect to the needle guide.
3. Measure the approximate transverse, axial, and sagittal distances from the origin of the needle guide to the target lesion on the CT console or workstation.
4. Use the needle insertion location equations (1) – (6) to determine the insertion locations and the insertion depth. (This step may be semi-automated)
5. Insert the needle into the calculated locations of the needle guide by measuring distance from the origin using the 1 cm spacing between the gridlines, stopping insertion just after traversing the skin.
6. Perform another CT scan in the same respiratory cycle to confirm the needle is aligned with the target lesion. If yes, continue to step 7. If no, repeat steps 3 – 6.
7. Continue pushing the needle the entire calculated insertion depth to contact the target lesion.

8. Perform another CT scan to confirm the target lesion is on track to be sampled (depending upon forward throw gun versus one snap gun). If yes, collect sample and remove the needle from the patient. If no, retract the needle and repeat steps 6 & 7.

Validation of Targeting Accuracy

An abdominal phantom was used to perform lesion-targeting experiments (n = 30) to validate the accuracy of the needle guide (Fig. 2.3a). The phantom consisted of a 3D printed outer shell with a soft plastic filling designed to match the density of human fatty tissue. The phantom contained various soft 3D printed tumors located throughout the abdominal cavity which were used as targets for needle insertions. The needle guide was positioned in the ventral insertion window of the phantom and the origin of the needle guide was aligned with the CT laser to assure proper craniocaudal angulation. After initial scans, the insertion locations and the insertion depth were calculated, and the biopsy needle (18-gauge x 200 mm) was inserted. Using confirmation scans, transverse, sagittal, and coronal distance errors were calculated from coordinates of CT images based on the distance between the needle tip and the center of the target tumor (Fig. 2.3d). Total error was calculated as the root mean square (RMS) distance of the transverse,sagittal, and coronal errors.

(a) 3D printed abdominal phantom for quantification of the lesion targeting error

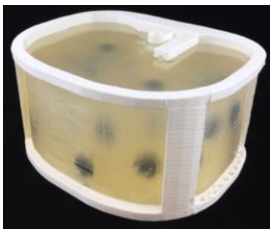

(b) Needle being inserted into the phantom using the origami needle guide

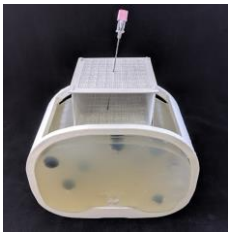

(c) CT image showing needle insertion through the origami needle guide into the abdominal phantom

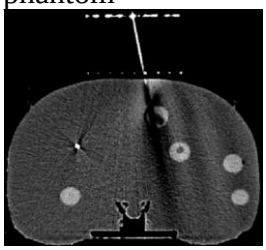

(d) Targeting errors were measured in transverse, sagittal, and coronal directions of the needle relative to the target lesion

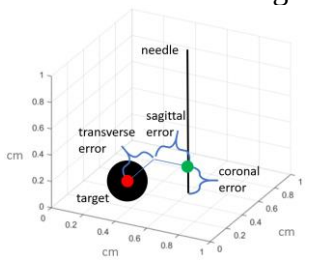

Figure 2.3. Abdominal phantom used for lesion targeting with the origami needle guide.

Device Analysis and Validation

Workspace Analysis

Fig. 2.4 shows the possible needle trajectories in the transverse plane provided by the gridlines on the origami lesion targeting device. The discrete potential insertion locations correspond to RCA gridlines. The RCA grids provide a high density of discrete guidelines, while the puncturable device material offers a continuous workspace for potential needle insertions.

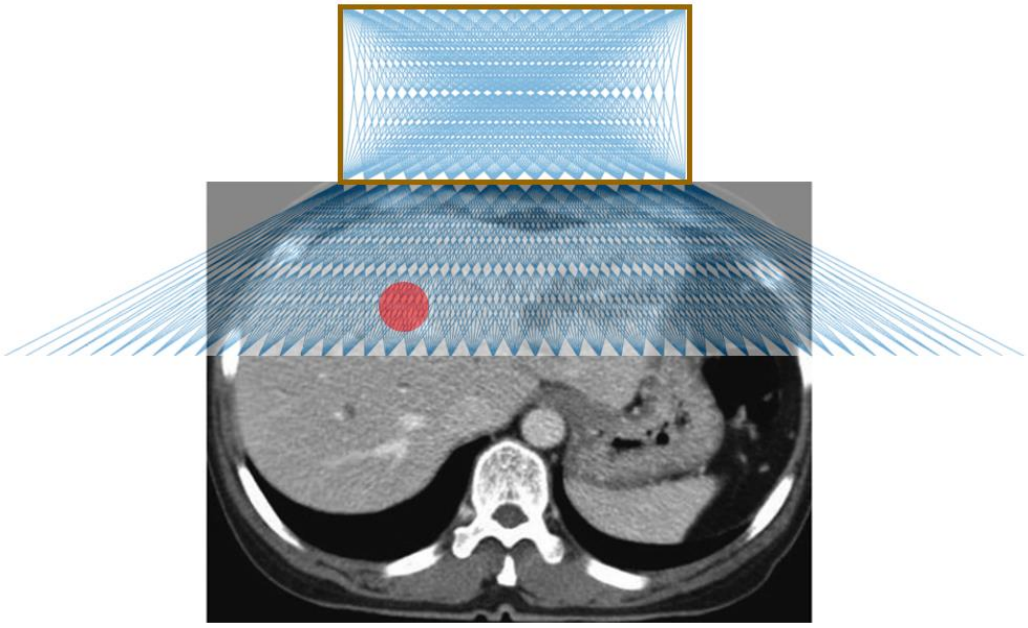

Figure 2.4. Illustration of possible needle trajectories in the transverse plane. The brown square represents the lesion targeting device, the red circle represents the target lesion, and the blue lines represent the needle trajectories.

Phantom Study

The results of the needle insertion experiments performed on an abdominal phantom are displayed in Fig. 2.5. Preliminary results showed successful CT-guided biopsy needle placements in an abdominal phantom. The mean targeting accuracy over all experiments was 2.51 mm (SD 0.59 mm, n=30). Voxel size for the images used in these calculations was 0.43 mm x 0.43 mm x 1.0mm. Fig. 2.5a displays a box and whisker plot comparing the targeting error between the sagittal, transverse, and coronal axes, Fig. 2.5b depicts the radial error, and Fig. 2.5c shows a Bland-Altman plot of the sagittal and transverse error measurements. The results show that the error was relatively evenly distributed around the target.

(a) Quartile plot of sagittal, transverse, coronal and total targeting error

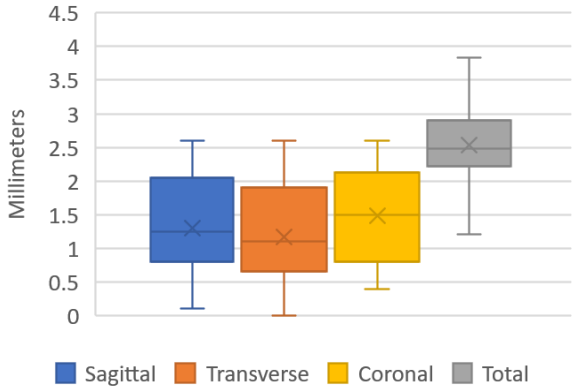

(b) Plot of radial error. Solid rings every millimeter, dashed rings every 0.5 mm

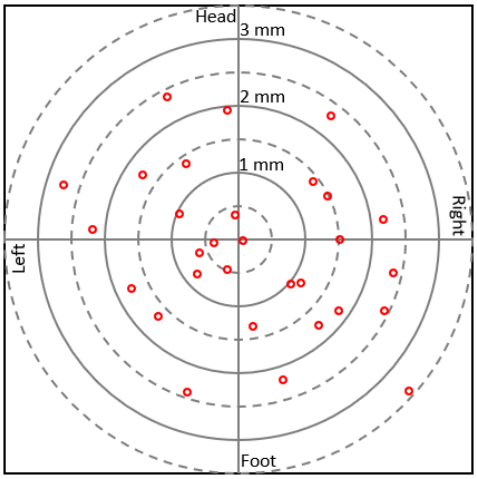

(c) Bland-Altman plot of sagittal and transverse error measurements

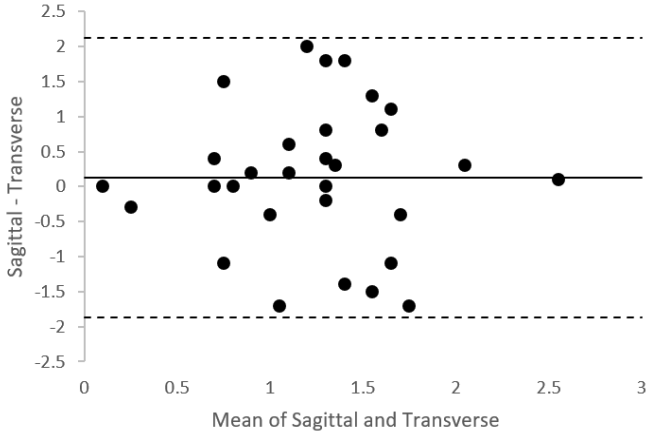

Figure 2.5. Plots of the lesion targeting error in phantom studies.

Discussion

The origami lesion targeting device provides several potential benefits for CT-guided percutaneous biopsy. One primary advantage is that since the device attaches to

the patient, it allows for the needles to move with the movement of the patient, thus potentially reducing the risk of tissue laceration by rigidly held needles. Another major benefit is that the device allows for multiple needles to be inserted, making it applicable for composite ablation using multiple electrodes. Furthermore, the device has the potential to guide off-axial needle insertion for highly inaccessible lesions that require multiple plane angulations. In addition to the potential benefits, the device can be manufactured quickly and inexpensively, making it disposable and therefore ideal for the surgical environment.

The device does not achieve as high of a degree of targeting accuracy as state-of-the-art computer-aided and robotic navigation systems. However, it provides smaller hospitals with an effective alternative where computer-aided and robotic navigation systems are not available. Moreover, the device does not require system set-up, instrument calibration, registration, and familiarity with the system to obtain optimal accuracy, as required with computer-aided and robotic systems.

Our preliminary evaluation exposed several limiting characteristics. The fixed nature of the needle guide may be disadvantageous in situations where the target lesion moves with time, such as with pulmonary lesions during respiration. Change to free-hand insertion as necessary may be prohibited without removing the needle from in-vivo and detaching the device from the patient. The flat surface of the device makes it unsuitable for accessing lesions which require a lateral approach, limiting it to be used mainly for abdominal procedures. Another limitation is that the large footprint of the device can make it difficult to be used with ultrasound. In future work, the device will be evaluated with in-vivo insertion and options for mitigating the effects of respiratory movement of

the target will be explored. The ability to guide multiple needles and off-axial needle insertion will also be evaluated. Iodine-based radiocontrast agents as well as other biocompatible materials will be explored. Additionally, the biocompatibility and hemocompatibility regulatory issues of having the needle traverse the material must to be certified. Given the limitations of the methodology, more rigorous testing in a specific clinical application would be necessary to compare this device with established systems.

A novel device for assisting with CT-guided needle insertions is presented. The device was fabricated by laser cutting the structure from a sheet of medical grade paperboard, 3D printing two radiocontrast agent grids on to the surface and folding the structure into a rectangular prism with a viewing window. The device was evaluated through CT imaging and targeting of lesions for needle insertions in an abdominal imaging phantom. The results of the lesion targeting experiments showed a mean targeting error of 2.53 mm (SD 0.59 mm, n=30). The main advantages of the device are that it attaches to the patient (potentially reducing the risk of laceration), it supports insertion of multiple needles (making it particularly suitable for composite ablations), and it can guide off-axial needle insertion. The low-cost and disposability characteristics make the device well-suited for interventional settings.

References

[1] K. Katada *et al.*, "Guidance with real-time CT fluoroscopy: early clinical experience," *Radiology*, vol. 200, no. 3, pp. 851-856, 1996.

[2] H. Li, P. M. Boiselle, J. Shepard, B. Trotman-Dickenson, and T. McLoud, "Diagnostic accuracy and safety of CT-guided percutaneous needle aspiration

biopsy of the lung: comparison of small and large pulmonary nodules," *AJR. American journal of roentgenology*, vol. 167, no. 1, pp. 105-109, 1996.

[3] S. G. Leffler and F. S. Chew, "CT-guided percutaneous biopsy of sclerotic bone lesions: diagnostic yield and accuracy," *AJR. American journal of roentgenology*, vol. 172, no. 5, pp. 1389-1392, 1999.

[4] S. N. Goldberg, M. T. Keogan, and V. Raptopoulos, "Percutaneous CT-guided biopsy: improved confirmation of sampling site and needle positioning using a multistep technique at CT fluoroscopy," *Journal of computer assisted tomography*, vol. 24, no. 2, pp. 264-266, 2000.

[5] E. vanSonnenberg *et al.*, "Difficult thoracic lesions: CT-guided biopsy experience in 150 cases," *Radiology*, vol. 167, no. 2, pp. 457-461, 1988.

[6] M. K. Mody, E. A. Kazerooni, and M. Korobkin, "Percutaneous CT-guided biopsy of adrenal masses: immediate and delayed complications," *Journal of computer assisted tomography*, vol. 19, no. 3, pp. 434-439, 1995.

[7] C. C. Wu, M. M. Maher, and J.-A. O. Shepard, "Complications of CT-guided percutaneous needle biopsy of the chest: prevention and management," *American Journal of Roentgenology*, vol. 196, no. 6, pp. W678-W682, 2011.

[8] P. Loubeyre, M. Copercini, and P.-Y. Dietrich, "Percutaneous CT-guided multisampling core needle biopsy of thoracic lesions," *American Journal of Roentgenology*, vol. 185, no. 5, pp. 1294-1298, 2005.

[9] M. Bernardino *et al.*, "CT-guided adrenal biopsy: accuracy, safety, and indications," *American journal of roentgenology*, vol. 144, no. 1, pp. 67-69, 1985.

[10] A. Olscamp, J. Rollins, S. S. Tao, and N. A. Ebraheim, "Complications of CT-guided biopsy of the spine and sacrum," *Orthopedics,* vol. 20, no. 12, pp. 1149-1152, 1997.

[11] K. Brabrand *et al.*, "Multicenter evaluation of a new laser guidance system for computed tomography intervention," *Acta Radiologica,* vol. 45, no. 3, pp. 308-312, 2004.

[12] V. Jacobi, A. Thalhammer, and J. Kirchner, "Value of a laser guidance system for CT interventions: a phantom study," *European radiology,* vol. 9, no. 1, pp. 137-140, 1999.

[13] Z. Varro, J. K. Locklin, and B. J. Wood, "Laser navigation for radiofrequency ablation," *Cardiovascular and interventional radiology,* vol. 27, no. 5, pp. 512-515, 2004.

[14] A. Magnusson, E. Radecka, M. Lönnemark, and H. Raland, "Computed-tomography-guided punctures using a new guidance device," *Acta Radiologica,* vol. 46, no. 5, pp. 505-509, 2005.

[15] C. Roberts, W. Morrison, D. Deely, A. Zoga, G. Koulouris, and C. Winalski, "Use of a novel percutaneous biopsy localization device: initial musculoskeletal experience," *Skeletal radiology,* vol. 36, no. 1, pp. 53-57, 2007.

[16] J. M. Henderson, K. L. Holloway, S. E. Gaede, and J. M. Rosenow, "The application accuracy of a skull-mounted trajectory guide system for image-guided functional neurosurgery," *Computer Aided Surgery,* vol. 9, no. 4, pp. 155-160, 2004.

[17] L. Appelbaum, J. Sosna, Y. Nissenbaum, A. Benshtein, and S. N. Goldberg, "Electromagnetic navigation system for CT-guided biopsy of small lesions," *American Journal of Roentgenology*, vol. 196, no. 5, pp. 1194-1200, 2011.

[18] V. Martens, S. Schlichting, A. Besirevic, and M. Kleemann, "LapAssistent—a laparoscopic liver surgery assistance system," in *4th European Conference of the International Federation for Medical and Biological Engineering*, 2009, pp. 121-125: Springer.

[19] H. Zhang *et al.*, "Electromagnetic tracking for abdominal interventions in computer aided surgery," *Computer Aided Surgery*, vol. 11, no. 3, pp. 127-136, 2006.

[20] F. Banovac *et al.*, "Precision targeting of liver lesions using a novel electromagnetic navigation device in physiologic phantom and swine," *Medical physics*, vol. 32, no. 8, pp. 2698-2705, 2005.

[21] K. Cleary, H. Zhang, N. Glossop, E. Levy, B. Wood, and F. Banovac, "Electromagnetic tracking for image-guided abdominal procedures: Overall system and technical issues," in *Engineering in Medicine and Biology Society, 2005. IEEE-EMBS 2005. 27th Annual International Conference of the*, 2006, pp. 6748-6753: IEEE.

[22] B. J. Wood *et al.*, "Navigation with electromagnetic tracking for interventional radiology procedures: a feasibility study," *Journal of vascular and interventional radiology*, vol. 16, no. 4, pp. 493-505, 2005.

[23] D. J. Grand, M. A. Atalay, J. J. Cronan, W. W. Mayo-Smith, and D. E. Dupuy, "CT-guided percutaneous lung biopsy: comparison of conventional CT fluoroscopy

to CT fluoroscopy with electromagnetic navigation system in 60 consecutive patients," *European journal of radiology,* vol. 79, no. 2, pp. e133-e136, 2011.

[24] B. C. Meyer *et al.*, "Electromagnetic field-based navigation for percutaneous punctures on C-arm CT: experimental evaluation and clinical application," *European radiology,* vol. 18, no. 12, p. 2855, 2008.

[25] C. K. Narsule *et al.*, "The efficacy of electromagnetic navigation to assist with computed tomography-guided percutaneous thermal ablation of lung tumors," (in eng), *Innovations (Phila),* vol. 7, no. 3, pp. 187-90, May-Jun 2012.

[26] T. Penzkofer *et al.*, "Free-hand CT-based electromagnetically guided interventions: accuracy, efficiency and dose usage," *Minimally Invasive Therapy & Allied Technologies,* vol. 20, no. 4, pp. 226-233, 2011.

[27] R. S. Santos *et al.*, "Electromagnetic navigation to aid radiofrequency ablation and biopsy of lung tumors," *The Annals of thoracic surgery,* vol. 89, no. 1, pp. 265-268, 2010.

[28] L. Maier-Hein *et al.*, "Precision targeting of liver lesions with a needle-based soft tissue navigation system," in *International Conference on Medical Image Computing and Computer-Assisted Intervention,* 2007, pp. 42-49: Springer.

[29] R. Bale *et al.*, "A novel vacuum immobilization device and a novel targeting device for computer assisted interventional procedures," in *CARS 2002 Computer Assisted Radiology and Surgery*: Springer, 2002, pp. 92-97.

[30] N. D. Glossop, "Advantages of optical compared with electromagnetic tracking," *JBJS,* vol. 91, no. Supplement_1, pp. 23-28, 2009.

[31] S. Tovar-Arriaga, R. Tita, J. C. Pedraza-Ortega, E. Gorrostieta, and W. A. Kalender, "Development of a robotic FD-CT-guided navigation system for needle placement—preliminary accuracy tests," *The International Journal of Medical Robotics and Computer Assisted Surgery*, vol. 7, no. 2, pp. 225-236, 2011.

[32] R. Pollock *et al.*, "Prospects in percutaneous ablative targeting: comparison of a computer-assisted navigation system and the AcuBot Robotic System," *Journal of endourology*, vol. 24, no. 8, pp. 1269-1272, 2010.

[33] G. Kronreif, M. Fürst, J. Kettenbach, M. Figl, and R. Hanel, "Robotic guidance for percutaneous interventions," *Advanced Robotics*, vol. 17, no. 6, pp. 541-560, 2003.

[34] A. Melzer, B. Gutmann, A. Lukoschek, M. Mark, W. Zylka, and H. Fischer, "Experimental evaluation of an MRI compatible telerobotic system for CT MRI guided interventions," *Supplement to Radiology*, vol. 226, p. 409, 2003.

[35] Y. Zhou, K. Thiruvalluvan, L. Krzeminski, W. H. Moore, Z. Xu, and Z. Liang, "CT-guided robotic needle biopsy of lung nodules with respiratory motion–experimental system and preliminary test," *The International Journal of Medical Robotics and Computer Assisted Surgery*, vol. 9, no. 3, pp. 317-330, 2013.

[36] B. J. J. Abdullah *et al.*, "Robot-assisted radiofrequency ablation of primary and secondary liver tumours: early experience," *European radiology*, vol. 24, no. 1, pp. 79-85, 2014.

[37] B. Schulz *et al.*, "Accuracy and speed of robotic assisted needle interventions using a modern cone beam computed tomography intervention suite: a phantom study," *European radiology*, vol. 23, no. 1, pp. 198-204, 2013.

[38] S. Groetz, K. Wilhelm, W. Willinek, C. Pieper, H. Schild, and D. Thomas, "A new robotic assistance system for percutaneous CT-guided punctures: initial experience," *Minimally Invasive Therapy & Allied Technologies,* vol. 25, no. 2, pp. 79-85, 2016.

[39] J. Kettenbach and G. Kronreif, "Robotic systems for percutaneous needle-guided interventions," *Minimally Invasive Therapy & Allied Technologies,* vol. 24, no. 1, pp. 45-53, 2015.

[40] J. Kettenbach, L. Kara, G. Toporek, M. Fuerst, and G. Kronreif, "A robotic needle-positioning and guidance system for CT-guided puncture: Ex vivo results," *Minimally invasive therapy & allied technologies,* vol. 23, no. 5, pp. 271-278, 2014.

[41] A. J. Megibow and M. A. Bosniak, "Dilute barium as a contrast agent for abdominal CT," *American Journal of Roentgenology,* vol. 134, no. 6, pp. 1273-1274, 1980.

CHAPTER 3

RAPID PROTOTYPING OF CUSTOM RADIOCONTRAST AGENT MARKERS

Radiocontrast Agent Skin Markers

Contrast agent skin markers are commonly used to identify areas of interest or to provide points of reference for a physician during image-guided procedures. Prior to accessing an internal lesion site of a patient for the purpose of inspection or therapeutic treatment, it is essential to learn the precise spatial information concerning the lesion site with respect to a reference position on the surface of the patient's body to avoid or alleviate damage of healthy tissues and enhance the outcome of such a medical treatment. A practicable method for attaining information concerning the spatial positioning of the lesion site is to apply a skin marker which gives a discriminative or distinctive view concurrently with imaging of the internal lesion, and to image the skin marker and the lesion site through a tomographic method so that the spatial interrelation between the images is determined.

Contrast agent skin markers are generally developed by combining a contrast agent with some sort of medium. Contrast agents are substances typically used to enhance the visibility of internal structures. X-ray based imaging techniques such as computed tomography (CT), projectional radiography, and fluoroscopy use radiocontrast agents to enhance imaging capabilities, while magnetic resonance imaging (MRI) uses gadolinium-based contrast agents which work by altering the magnetic properties of nearby hydrogen nuclei. Radiocontrast agents are typically iodine or barium-sulphate-based compounds.

Iodinated contrast agents are the main type of radiocontrast used for intravenous administration, while barium sulfate is mainly used in the imaging of the digestive system.

Previous reports have described the use of angiocatheters [1, 2] or thermoplastic resin shells [3] as markers. These markers are produced by dispersing a radiopaque material throughout the walls of the catheter or shell. These techniques, however, provide only an approximate estimate of cancer extension and are extremely difficult to use. In comparison, skin markers have been shown to provide precise information about tumor location, while offering ease of use [4-9]. Various radiopaque skin markers include pellets, crosshairs, and grids [10]. In addition to creating custom 2D skin markers, it is show that 3D markers which can be used to facilitate needle targeting of lesions can be developed.

In the following sections, details of the development of custom radiocontrast skin markers are presented, including radiocontrast agent mixture design, printing the radiocontrast agent mixture, and developing various 2D radiocontrast agent skin markers and 3D radiocontrast agent needle guides. CT images of the custom radiocontrast agent skin markers and needle guides were taken to verify the visibility of the contrast agent. Printing performance was quantified in terms of line width variation, infill percentage, and roundness.

System Design

Development of a Custom Radiocontrast Agent Mixture

The radiocontrast agent mixture was developed with three major design criteria in mind. The first and most important goal was for the mixture to be bright enough to show up in a CT scan. Secondly, the mixture needed to be able to be stored and extruded as a liquid and transition into a solid upon exposure to air. Lastly, the radiocontrast agent

mixture required a viscosity which would allow it to be extruded through a 1 mm diameter orifice in a controlled manner. The resulting mixture was 80 wt % Elmer's glue, 10 wt % barium sulfate, and 10 wt % water, which gave sufficient visibility within the CT images and adequate viscosity for printing. Barium sulfate (Hi-LR) from HiMedia Laboratories was chosen as the radiocontrast agent due to its exceptional radiopacity [11].

Design of a Method for Printing Radiocontrast Agent Mixture

To increase manufacturability and to decrease fabrication time, the radiocontrast agent mixture was printed. A Fisher Scientific syringe pump (Fig. 3.1a) was used to extrude the mixture from an EXELINT 50 mL Luer Lock Tip syringe at a constant rate of 200 mL/hr. A 5 mm diameter tube connected the syringe to a 1 mm blunted needle which was mounted to the head of a Full Spectrum laser cutter. The needle was mounted vertically on the head of the laser cutter, leaving 1 mm of spacing between the needle tip and the printing substrate (Fig. 3.1b). The laser cutter uses computer numeric control (CNC) to move the extruder head along the path of the desired shape (Fig. 3.1c). Since the syringe pump and CNC are controlled separately, the pump was manually turned on and off when the print job started and finished. Fig. 3.2 shows a schematic diagram of the experimental setup.

(a) Syringe pump | (b) Needle tip mounted to laser cutter head | (c) Printing radiocontrast agent mixture

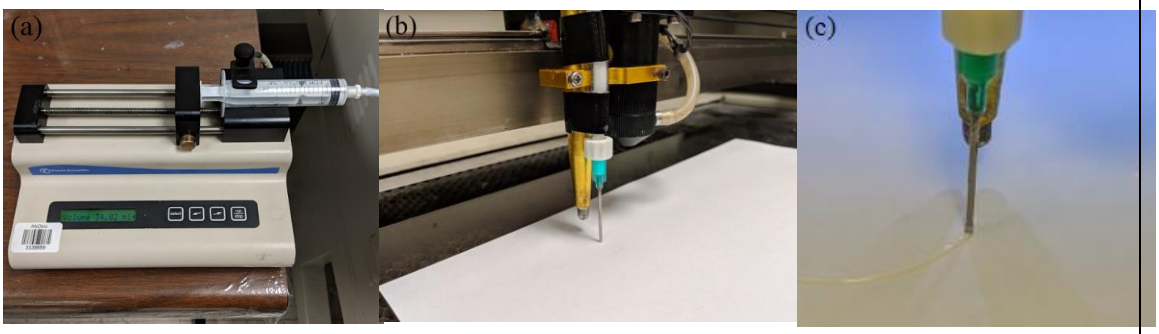

Figure 3.1. Radiocontrast agent mixture printing setup.

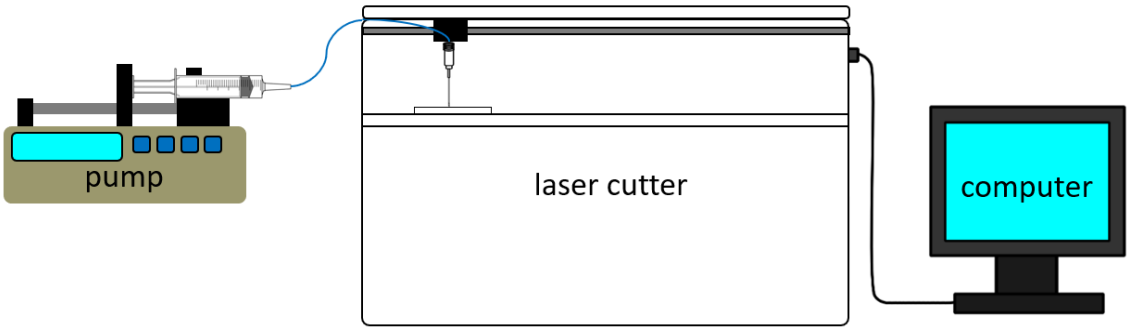

Figure 3.2. Schematic diagram of the experimental setup.

Printing Custom Radiocontrast Agent

The radiocontrast agent markers can easily be customized for a specific patient or procedure as the desired shape of the marker is drawn using AutoCAD. Fig. 3.3 shows the AutoCAD drawings of a circle, a solid square, and an angle pattern at with lines at 10º intervals. The CAD files were uploaded to the laser cutter software, RetinaEngrave, where the specific CNC tool path was defined, and the laser power was turned off. Notice how the solid square and the angled pattern are a single connected line. This is because the mixture is being extruded the entire time from start to finish of the CNC job. This puts a significant limitation on the designs that can be printed and is a major area of focus for future work on this project.

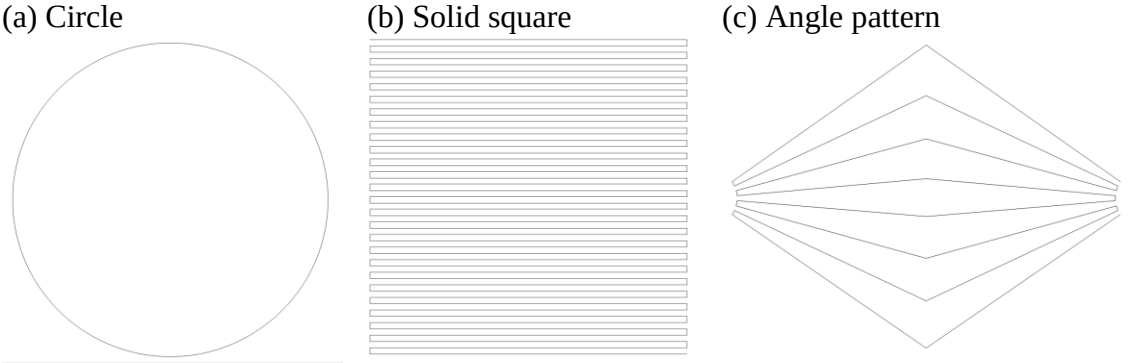

Figure 3.3. AutoCAD drawing of various CT markers.

The two most important aspects regarding the fabrication of the custom radiocontrast agent markers are the volume of material required and the time taken to print

the various CT markers. The 3D printing literature suggests that the key variables to consider are the critical nozzle height hc, the flow rate Q, nozzle diameter D_n, and the nozzle movement speed v_n [12-14]. Wang and Shaw gave an equation to estimate critical nozzle height as

$$h_c = \frac{Q}{v_n D_n} \tag{1}$$

Yang et al. found that the nozzle height is suitable to be the same as the nozzle diameter. The extrusion rate and the nozzle movement speed affect the 3D printing simultaneously, both affecting the amount of extrusion per unit length per unit time. Khalil et al. show that for a given flow rate Q and a given time t the volume extruded from the nozzle system V can be calculated as

$$V = Qt \tag{2}$$

Assuming the extruded volume forms a cylindrical strut of uniform diameter D with a length L,

$$V = \pi \left(\frac{D}{2}\right)^2 L \tag{3}$$

For a given time t and movement speed vn,

$$L = v_n t \tag{4}$$

Combining Eqs. (1) – (3) yields

$$v_n = \frac{4Q}{\pi D^2} \tag{5}$$

Combining Eqs. (2) and (5) yields

$$V = \frac{Q*L}{v_n} \tag{6}$$

The printing of the radiocontrast agent was evaluated by characterizing the roundness of the printed circle, the infill percentage of the solid square, and the print resolution standard deviation. To calculate the deviation in roundness, a single trace covering the full rotation was made, and at N equally spaced angles θ_i, a measurement R_i, of the radius or distance between the center of rotation and the surface point is taken. A least-squares fit to the data gives the following estimators of the parameters of the circle:

$$\Delta = R_i - R - a\cos\theta - b\sin\theta_i \tag{7}$$

where

$$R = \frac{1}{N}\sum_{i=1}^{N} R_i \tag{8}$$

$$a = \frac{2}{N}\sum_{i=1}^{N} R_i \cos\theta_i \tag{9}$$

$$b = \frac{2}{N}\sum_{i=1}^{N} R_i \sin\theta_i \tag{10}$$

Table 3.1 shows the nomenclature for the symbols used in the equations above.

Table 3.1. Symbol Nomenclature for RCA Printing Equations

Symbol	**Variable**	**Unit**
h_c	Nozzle height	mm
Q	Flow rate	mL/s
Dn	Nozzle diameter	mm
v_n	Nozzle movement speed	mm/s
V	Extruded volume	mL
t	Time	s
D	Diameter of cylindrical strut	mm
L	Print length	mm
θ_i	Angle	degrees
R_i	Radius	mm
N	Number of measurements	none

Development of 2D Radiocontrast Skin Markers and 3D Radiocontrast Needle Guides

The radiocontrast agent was printed onto a medical grade paper. Fig. 3.4 shows the completed prototypes of the various radiocontrast agent markers. After printing the

radiocontrast agent in the desired pattern onto the substrate, double sided adhesive was applied to the bottom of the substrate to provide an effective means of attaching the markers to a patient. Figs. 3.4a and 3.4b show the 2D circular and square skin markers, respectively. Fig. 3.4c shows the 3D skeletal pyramid which demonstrates the ability to print several 2D patterns on separate substrates and combine them together to develop novel 3D structures. The 3D skeletal pyramid was folded from four separate sheets of paper, three of which contained printed radiocontrast agent.

(a) Circular skin marker (b) Solid square skin marker (c) 3D skeletal pyramid needle guide

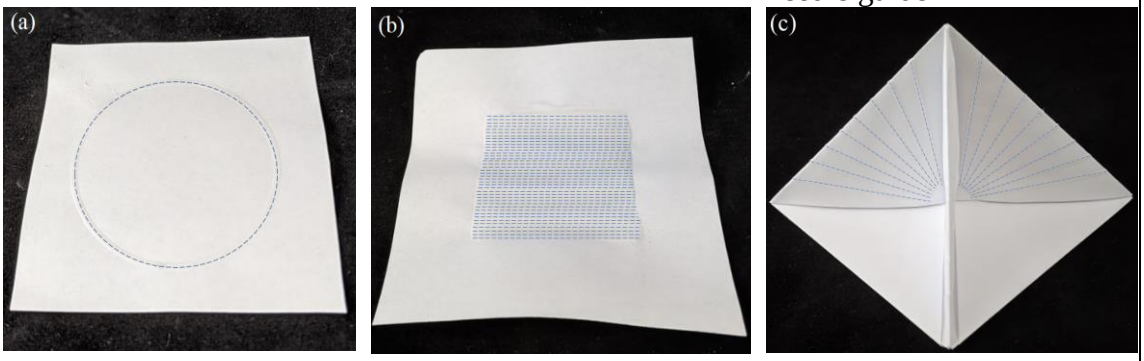

Figure 3.4. Various radiocontrast agent skin markers. Dashed lines highlight the printed radiocontrast agent.

System Analysis and Evaluation

Evaluation of Nozzle Diameter and Nozzle Movement Speed

The nozzle diameter directly governs the print resolution and the time taken to print markers. Various nozzle diameters were evaluated to compare the time taken to print the solid square marker. As shown in Fig. 3.5, the smaller the nozzle diameter, the greater the time taken to print the solid square marker. There was a significant increase in time from the 1.0 mm nozzle to the 0.5 mm nozzle. For our application, the 1.0 mm nozzle provided the best print resolution without sacrificing significant print time.

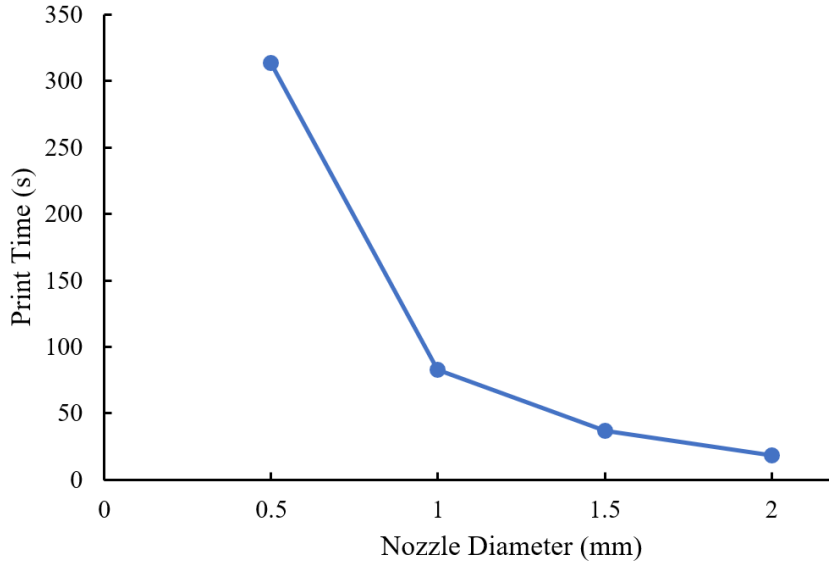

Figure 3.5. Time taken to print the solid square marker with various nozzle diameters.

Radiocontrast Agent Printing Evaluation

Using Eqs. (7) – (10), the deviation in roundness was calculated to be 0.23 mm (N = 30).

The infill percentage was calculated by measuring the area of the space unfilled by radiocontrast agent within the solid square shape and subtracting it from the total area of the shape. The infill percentage was calculated to be approximately 99.9%.

The average line thickness of the printed radiocontrast agent lines was calculated by measuring the average line thickness of the 32 lines on the skeletal pyramid 3D needle guide. The lines were each 10 mm in length and measurements were taken at 10 different locations along the lines, for a total of 320 measurements. Fig. 3.6 shows a scatter plot of the average thickness of the 32 different lines. The average line thickness was calculated to be 1.56 mm with a standard deviation of ± 0.19 mm.

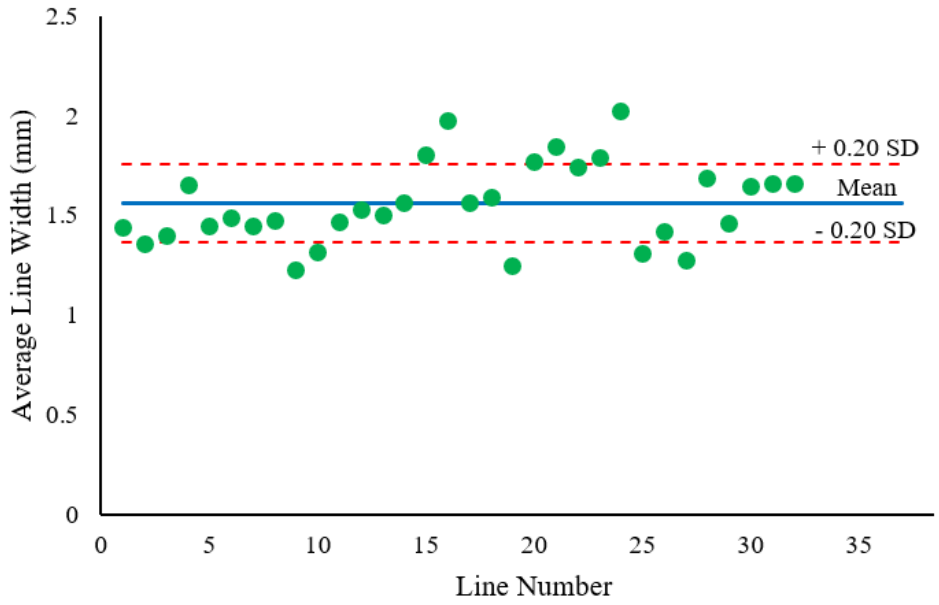

Figure 3.6. Scatter plot showing the measurements of the average line thickness of the 32 different lines printed on the skeletal pyramid needle guide.

Table 3.2 shows the calculated radiocontrast agent mixture volume and the time required to print the circle, solid square, and skeletal pyramid needle guide.

Table 3.2. Radiocontrast Agent CT Marker Print Characteristics

Shape	Extrusion Rate (mL/s)	Speed (mm/s)	Length (mm)	Print Volume (mL)	Print Time (s)
Circle	0.056	30	157	0.29	5.23
Square	0.056	30	2500	4.67	83.33
Pyramid	0.056	30	1600	2.99	53.33

Radiocontrast Agent Marker CT Images

The three prototype radiocontrast agent markers were each imaged in a CT scanner with 0.6 mm slice thickness. Fig. 3.7 shows a single slice of each of the prototypes. The slices in Figs. 3.7a and 3.7b were taken in the coronal plane while the slice in Fig. 3.7c was taken in the transverse plane. The dark waves in the Fig. 3.7b are due to the bending of the paper, which was a result of the radiocontrast agent mixture seeping into the paper and

degrading the structural integrity. Thicker paper or a wax coating would help to mitigate this negative effect. The solid square has some beam hardening artifacts that would likely also be mitigated with a substrate of greater resistance to warping upon interaction with a liquid.

(a) Circular skin marker (b) Solid square skin marker (c) Skeletal pyramid needle guide

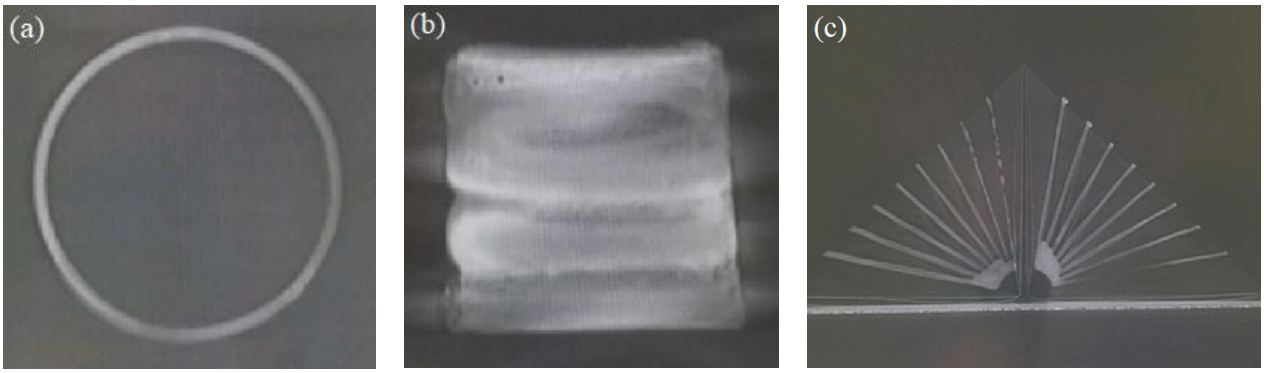

Figure 3.7. CT images of various radiocontrast agent markers.

Discussion

The development of a method for printing a custom radiocontrast agent mixture provides several potential benefits for CT-guided procedures. One primary advantage is the ability to print various markers of various sizes to provide the most optimal marker given the specific patient and procedure. Another major benefit is the ability to fold flat printed patterns into 3D structures which can serve to guide and support needle insertions. In addition, the markers can be fabricated quickly and inexpensively, making them disposable and therefore ideal for the surgical setting.

This study did not evaluate the use of the proposed skin markers in a clinical setting. Thus, the toxicity of the radiocontrast agent was not examined. This is a major area for future study because contrast agents can cause mild to severe reactions. Also, barium sulfate, the contrast agent used in this study, is typically delivered orally, where iodine-

based contrast agents are typically delivered intravenously. Future studies will aim to experiment with creating skin markers from iodine-based contrast agents.

Another major limitation of this study was the inability to control both the laser cutter CNC and the syringe pump together. This limited printing of the radiocontrast agent mixture to designs that are made from a single connected line. Future work will aim to connect the control circuit of the syringe pump to an external control unit which can sync together the control of the laser cutter CNC with the control of the syringe pump. In addition, once the syringe pump has been turned off, mixture continues to leak from the nozzle as the pressure built up in the tubing dissipates. Some sort of mechanism to instantly stop the extrusion would be beneficial for printing more complex patterns.

A novel method for printing a custom radiocontrast agent mixture is presented. The custom radiocontrast agent mixture was shown to be clearly visible within CT images, able to be stored in a liquid state and transition into a solid upon extrusion, and sufficiently viscous to flow through a tube and out a 1.0 mm nozzle in a controlled manner. The radiocontrast agent mixture was successfully printed via a syringe pump and CNC to allow for rapid development of patient-specific CT markers. In addition to printing 2D CT skin markers, it was shown that the substrate on which the radiocontrast agent mixture is printed can be folded into novel 3D structures which can serve to guide and support needle insertions. The resulting radiocontrast agent markers were shown to have clear visibility within CT images with minimal artifacts. The printing ability was evaluated to have 1.56 mm (SD 0.19 mm, n = 30) printing resolution, 99.9% infill in a solid shape, and a deviation in roundness of 0.23 mm (n = 30).

References

[1] D. P. Frush and J. R. Herlong, "Pediatric thoracic CT angiography," Pediatric radiology, vol. 35, no. 1, pp. 11-25, 2005.

[2] T. Inoue et al., "Usefulness of three-dimensional multidetector-row CT images for preoperative evaluation of tumor extension in primary breast cancer patients," Breast cancer research and treatment, vol. 89, no. 2, pp. 119-125, 2005.

[3] M. Makita, N. Gomi, and T. Tachikawa, "CT-guided Thermoplastic assisted segmentectomy is an optimal breast conserving surgery for breast cancer with nipple discharge," Nyugan No Rinsho, vol. 19, no. 2, pp. 142-149, 2004.

[4] N. Harada-Shoji et al., "Usefulness of lesion image mapping with multidetector-row helical computed tomography using a dedicated skin marker in breast-conserving surgery," European radiology, vol. 19, no. 4, p. 868, 2009.

[5] A. A. Khankan and M. Al-Muaikeel, "Image-guided percutaneous transthoracic biopsy in lung cancer–Emphasis on CT-guided technique," Journal of infection and public health, vol. 5, pp. S22-S30, 2012.

[6] W. Lee, S. Chong, J. Seo, and H. Shim, "Transthoracic fine-needle aspiration biopsy of the lungs using a C-arm cone-beam CT system: diagnostic accuracy and post-procedural complications," The British journal of radiology, vol. 85, no. 1014, pp. e217-e222, 2012.

[7] K. R. Birchard, "Transthoracic needle biopsy," in Seminars in interventional radiology, 2011, vol. 28, no. 01, pp. 087-097: © Thieme Medical Publishers.

[8] J. Krücker et al., "Clinical utility of real-time fusion guidance for biopsy and ablation," Journal of vascular and interventional radiology, vol. 22, no. 4, pp. 515-524, 2011.

[9] D. J. Grand, M. A. Atalay, J. J. Cronan, W. W. Mayo-Smith, and D. E. Dupuy, "CT-guided percutaneous lung biopsy: comparison of conventional CT fluoroscopy to CT fluoroscopy with electromagnetic navigation system in 60 consecutive patients," European journal of radiology, vol. 79, no. 2, pp. e133-e136, 2011.

[10] V. Huang, J. Kamarn, R. D'Arcy, and K. Kohli, "SU-G-IeP2-02: A Proposed Solution to Accurate Delineation of External Body Contour Within CT Extended Field of View (eFOV) and the Evaluation of Dosimetric Impact from Image Distortion in EFOV," Medical physics, vol. 43, no. 6Part26, pp. 3655-3656, 2016.

[11] A. J. Megibow and M. A. Bosniak, "Dilute barium as a contrast agent for abdominal CT," American Journal of Roentgenology, vol. 134, no. 6, pp. 1273-1274, 1980.

[12] F. Yang, M. Zhang, B. Bhandari, and Y. Liu, "Investigation on lemon juice gel as food material for 3D printing and optimization of printing parameters," LWT, vol. 87, pp. 67-76, 2018.

[13] J. Wang and L. L. Shaw, "Rheological and extrusion behavior of dental porcelain slurries for rapid prototyping applications," Materials Science and Engineering: A, vol. 397, no. 1-2, pp. 314-321, 2005.

[14] S. Khalil and W. Sun, "Biopolymer deposition for freeform fabrication of hydrogel tissue constructs," Materials Science and Engineering: C, vol. 27, no. 3, pp. 469-478, 2007.

CHAPTER 4

CT-GUIDED ABDOMINAL BIOPSY TRAINING PHANTOM

Percutaneous Biopsy

Percutaneous core-needle biopsy is widely considered a reliable method for accurate diagnosis of various medical conditions [1-4]. CT guidance considerably expands the scope of lesions amenable to percutaneous biopsy [5, 6]. A study conducted by Welch et al. [7] analyzed 1,000 biopsies of various types guided with CT and showed that 93% of cases were diagnosed accurately. The high spatial and contrast resolution of CT images can help to localize biopsy targets almost anywhere in the human body [8]. This creates a high demand for trained medical practitioners with expertise in CT-guided procedures. Complications associated with biopsies such as hemorrhage and perforation [9-12] can be reduced through proper biopsy training.

An abdominal biopsy phantom was designed to provide a means for training and demonstrating image-guided needle biopsy procedures that require a constant visual reference for needle placement. The CIRS abdominal biopsy phantom is an industry standard, so the proposed phantom was compared with the CIRS phantom [13]. Table 4.1 shows a comparison of the features of each of the abdominal phantoms. The key advantages that the proposed phantom offers are: (1) the ability to electromagnetically (EM) track lesion locations; (2) the capability to customize the size and shape of the phantom as well as the locations of the lesions to match patient-specific anatomy; and (3) the low cost of manufacturing.

Table 4.1. Comparison of CIRS Abdominal Phantom and the Proposed Abdominal Phantom

	CIRS phantom	**Proposed phantom**
Shell	Urethane	Polylactic acid (PLA)
Lesions	No tracking	EM tracking
Filling	Zerdine, 1550 m/s (nominal)	Super soft plastic/plastic softener
Customizable	No	Yes—patient-specific customization
Suitable for CT	Yes	Yes
Price	~ $2000 USD	< $100 USD

Abdominal Phantom Design

Shell Design

The shell of the phantom was designed in SolidWorks (Fig. 4.1a) and printed in polylactic acid (PLA) (Fig. 4.1b), a biodegradable thermoplastic, on a Makerbot Replicator printer. The shell model was designed to include two windows for needle insertion: one for insertion through the top, and one for insertion through the side. Fig. 4.1c shows the 3D printed shell with caps covering the windows. The window caps provide stability to the structure during filling pouring and transportation of the phantom.

(a) CAD model (b) 3D printed shell (c) Shell with window caps

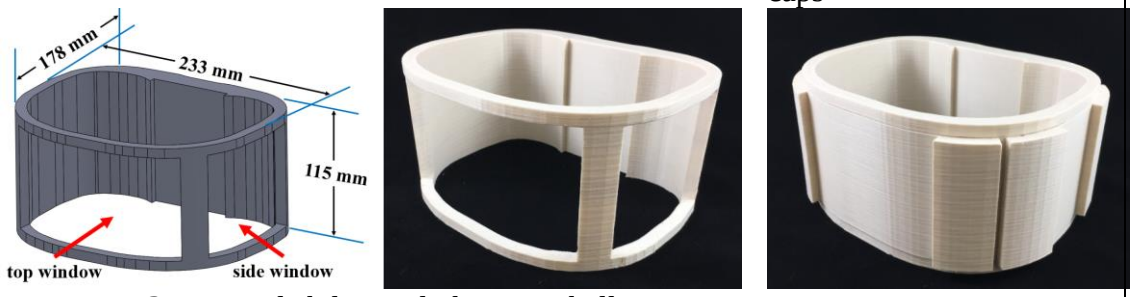

Figure 4.1. 3D printed abdominal phantom shell.

Lesion Design

Phantom lesions were designed in SolidWorks (Figs. 4.2a & 4.2b) and 3D printed in Formlabs' flexible material on a Form 2 printer (Fig. 4.2c). The spherical lesions have a 2 cm diameter and a 5 mm diameter cylindrical hole to allow for insertion of an electromagnetic (EM) tracking coil (Fig. 4.2d). They contain a hollow center between the outer wall and the inner cylindrical tube to allow the lesion to be more easily penetrated (Fig. 4.2b).

Specific locations for twelve lesions were randomly determined in the CAD model (Fig. 4.2e).

(a) Custom lesion CAD model

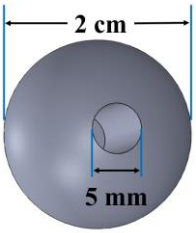

(b) Lesion CAD model cross-section

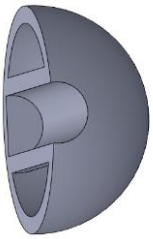

(c) 3D-printed custom lesion

(d) Tracking coil housed within lesion

(e) Abdominal phantom CAD model with defined lesion locations.

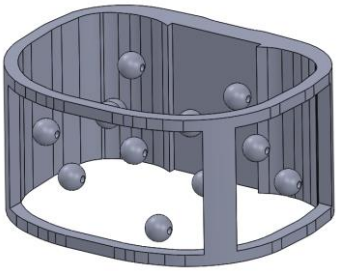

Figure 4.2. Custom lesion CAD model and 3D printed prototype.

Spine Model

A CAD model of a section of the human spine (Fig. 4.3a) was acquired from [14] and used to print a 3D model from PLA on a Makerbot Replicator printer (Fig. 4.3b). The spine model was scaled to the approximate size of an adult human spine and included inside the abdominal phantom.

(a) Spine CAD model (b) 3D printed spine model

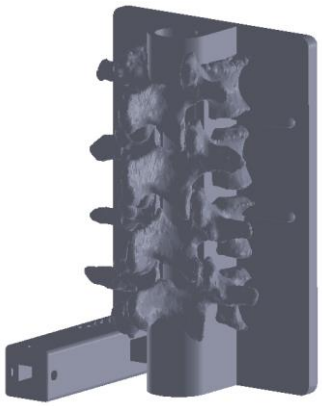

Figure 4.3. Spine CAD and 3D printed model.

Soft Plastic Filling Composition and Characteristics

The aim for the abdominal phantom filling was to simulate a true human abdomen by matching the density of the filling to that of the human abdominal tissue. According to [15], the density of human fatty tissue is approximately 911 kg/m3 and the density of human muscle tissue is approximately 1100 kg/m3.

The filling of the abdominal phantom was created from a mixture of super soft plastic [14], plastic softener [14], and a small amount of mineral oil (2%). The soft plastic and plastic softener were mixed together to create a gelatin-like material and the mineral oil was used to prevent the soft plastic from being too sticky. Density and penetrability were measured on ten different plastic mixture compositions with soft plastic to plastic

softener ratios ranging from 1:1 to 10:1 (Fig. 4.4a) to determine the composition that most closely resembled the human abdomen.

The ten filling samples were each cut into a uniform shape of a cylinder of 50 mm diameter and 33 mm height. The density was calculated by measuring mass and volume directly and dividing mass by volume. The penetrability was measured by dropping a weighted needle into the plastic mixture samples (Fig. 4.4b). A resistive force of approximately 0.5 N was chosen after consultation with an interventional radiologist to select a reasonable force to penetrate through abdominal organs. To achieve the 0.5 N force, a mass (50 g) was mounted to the end of the needle using a 3D-printed mount. To compare the experimental results to the industry standard in abdominal phantoms, the penetration depth of a CIRS abdominal biopsy phantom was tested.

(a) Ten samples of various ratios of super soft plastic and plastic softener

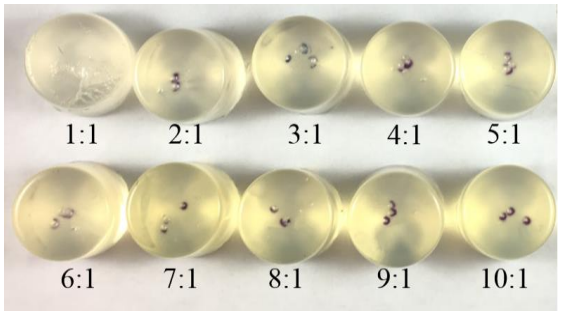

(b) Penetrability measurement experimental setup

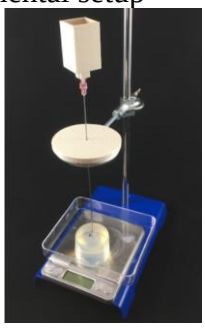

Figure 4.4. Soft plastic mixture composition experiments.

Abdominal Phantom Prototype and CT Scan

Once the optimal abdominal phantom filling composition was selected based on the experimental results shown in section 3.1, the phantom prototype was created. Twelve lesions were placed inside the phantom, with each location matching exactly to the dimensions of the CAD model (Fig. 4.5). The phantom was constructed in four layers of plastic filling in order to place the lesions at various heights. The prototype only

contained one EM tracking coil to prove the concept of EM tracked lesions, but future prototypes have the potential to contain an EM tracking coil in every lesion. The abdominal phantom prototype was scanned inside of a computed tomography (CT) scanner to observe its visibility in CT images.

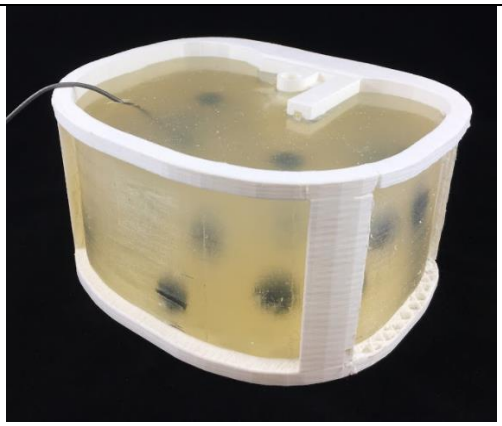

Figure 4.5. Completed abdominal phantom prototype with 12 lesions and 3:1 soft plastic to plastic softener composition.

The tracking coils used in this study were homemade and inexpensive to make (< $5). The cost of the entire prototype was approximately $60, which is a low cost for an effective method to train medical practitioners (Table 4.2).

Table 4.2. Breakdown of Custom Abdominal Phantom Costs

Item	Shell	Lesions	Spine	Filling	In-house designed EM tracker	**Total**
Cost	~$5	~$5	~$2	~$40	~$5	~$57

Tracking Coil Software

An Aurora EM Tracking System [16] was used to track both the lesion inside the phantom and the tip of a needle. The previously acquired CT images of the abdominal phantom were imported into OncoNav navigation software, which displayed the axial, sagittal, and transverse planes of the imported image set. The software allowed the user to

select a target point (target lesion) and the tip of the needle was indicated with crosshairs to help guide the user to the target location.

Needle Insertion Data

Five medical trainees practiced inserting a needle into the lesions of the abdominal phantom using CT guided imaging. Each trainee completed 10 trials of attempting to insert a needle into a lesion randomly selected by the experimenter. Each trial was measured by how many insertions/retractions it took for the trainee to hit the target lesion.

Abdominal Phantom Evaluation

Abdominal Phantom Soft Plastic Filling Characteristics

The density values of the filling samples ranged from 888 kg/m3 to 967 kg/m3 (Fig. 4.6a). The density of human fatty tissue lies within the soft plastic mixture density range, but future work is required to achieve a higher density to match that of human muscle tissue. The 3:1 soft plastic mixture was chosen for the prototype because it most closely resembled human fatty tissue.

The penetration depth of the CIRS abdominal biopsy phantom was 22 mm. The penetration depth in the filling samples decreased as the soft plastic to plastic softener ratio increased (Fig. 4.6b). The plot of the relationship shows that the penetration depth began to approach an asymptote around 10 mm.

(a) Density (kg/m^3) vs plastic mixture ratio

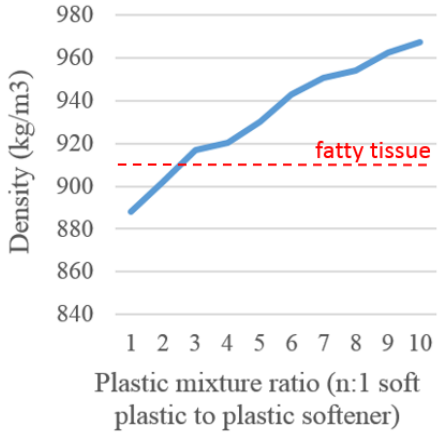

(b) Average penetration depth (mm) vs plastic mixture ratio with the industry standard CIRS abdominal phantom penetration depth displayed as a dashed line.

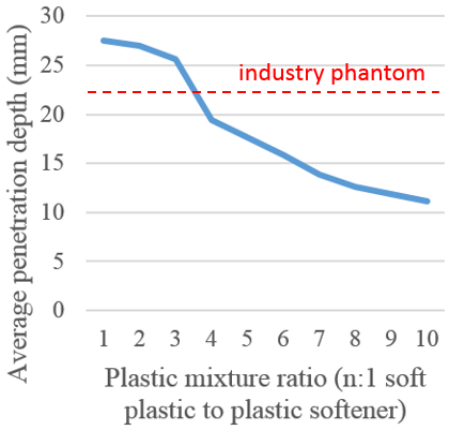

Figure 4.6. Soft plastic and plastic softener mixture properties. Plastic mixture is a composition of soft plastic and plastic softener (n:1).

Abdominal Phantom CT Scan

The CT scans of the phantom prototype showed that the shell of the phantom and its internal filling and lesions were clearly visible in CT images. The tracking coil created a bright spot in the CT image (Fig. 4.7), improving the visibility of the lesions to assist the practitioner in guiding the needle to the target lesion.

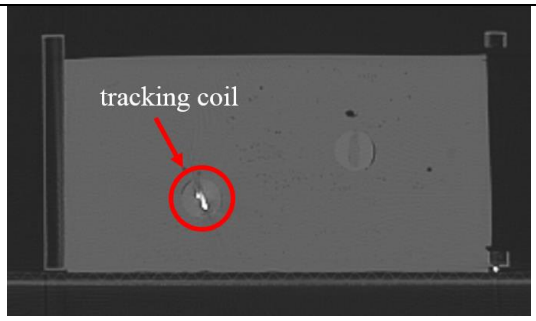

Figure 4.7. CT scanned image of abdominal phantom.

Tracking Coil Software

The OncoNav software successfully tracked the lesion and needle tip locations in CT scans of the abdominal phantom (Fig. 4.8).

Needle Insertion Experiments

In the 50 trials, 50 out of 65 total needle insertions to target lesions were successful, which was a success rate of 76.9%.

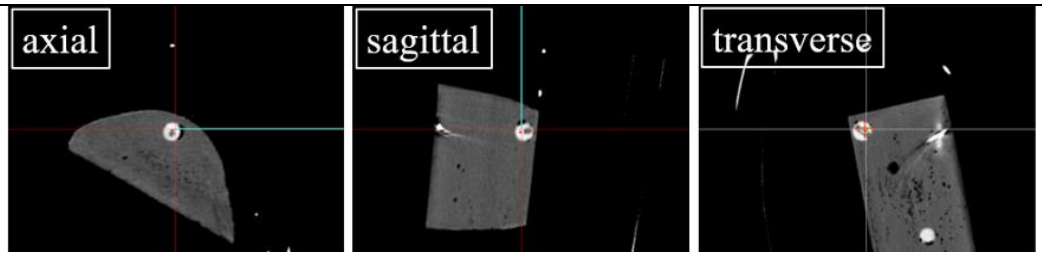

Figure 4.8. Lesion and needle tracking in OncoNav software. Crosshairs indicate tracked needle tip location.

Discussion

The abdominal phantom prototype developed in this study provides an inexpensive method for physicians to practice needle insertion with CT image guidance and EM tracking assistance. The CT images only need to be obtained once to be used for practice in office settings, making this device very suitable for interventional radiology training. The inner filling was designed to have a similar density to that of human fatty tissue to closely mimic an actual human body as closely as possible. The penetrability of the filling was analyzed to observe the relationship between the mixture composition ratio and the penetrability. In future work, the penetrability of human tissue will be measured to compare with experimental results from the proposed phantom. CT images of the abdominal phantom were taken to observe the visibility of the shell, the lesions, and the filling in CT images. The CT images were imported into OncoNav navigation

software and used for biopsy training with medical practitioners. The needle insertion lesion-contact data showed a 76.9% success rate in making contact with the target lesion upon insertion. Further research will aim to compare our data to needle insertion data on other industry standard abdominal phantoms as well as human tissue. Overall, the proposed abdominal phantom prototype provides a low-cost device to train physicians in CT-guided needle insertion procedures.

References

[1] R. Agid, M. Sklair-Levy, A. Bloom, S. Lieberman, A. Polliack, D. Ben-Yehuda, et al., "CT-guided biopsy with cutting-edge needle for the diagnosis of malignant lymphoma: experience of 267 biopsies," Clinical radiology, vol. 58, pp. 143-147, 2003.

[2] K. R. Brandt, J. Charboneau, D. Stephens, T. Welch, and J. Goellner, "CT-and US-guided biopsy of the pancreas," Radiology, vol. 187, pp. 99-104, 1993.

[3] F. Laurent, V. Latrabe, B. Vergier, M. Montaudon, J.-M. VERNEJOUX, and J. Dubrez, "CT-guided transthoracic needle biopsy of pulmonary nodules smaller than 20mm: results with an automated 20-gauge coaxial cutting needle," Clinical radiology, vol. 55, pp. 281-287, 2000.

[4] J. Schmidbauer, M. Remzi, M. Memarsadeghi, A. Haitel, H. C. Klingler, D. Katzenbeisser, et al., "Diagnostic accuracy of computed tomography-guided percutaneous biopsy of renal masses," European urology, vol. 53, pp. 1003-1012, 2008.

[5] E. vanSonnenberg, G. Casola, M. Ho, C. Neff, R. Varney, G. Wittich, et al., "Difficult thoracic lesions: CT-guided biopsy experience in 150 cases," Radiology, vol. 167, pp. 457-461, 1988.

[6] J. R. Haaga and R. J. Alfidi, "Precise biopsy localization by computed tomography," Radiology, vol. 118, pp. 603-607, 1976.

[7] T. Welch, P. Sheedy 2nd, C. Johnson, C. Johnson, and D. Stephens, "CT-guided biopsy: prospective analysis of 1,000 procedures," Radiology, vol. 171, pp. 493-496, 1989.

[8] K. Ahrar, "CT-Guided Biopsy," in Percutaneous Image-Guided Biopsy, ed: Springer, 2014, pp. 19-32.

[9] N. Tomiyama, Y. Yasuhara, Y. Nakajima, S. Adachi, Y. Arai, M. Kusumoto, et al., "CT-guided needle biopsy of lung lesions: a survey of severe complication based on 9783 biopsies in Japan," European journal of radiology, vol. 59, pp. 60-64, 2006.

[10] D. Lebrec, G. Goldfarb, C. Degott, B. Rueff, and J.-P. Benhamou, "Transvenous liver biopsy," Gastroenterology, vol. 83, pp. 338-340, 1982.

[11] M. K. Mody, E. A. Kazerooni, and M. Korobkin, "Percutaneous CT-guided biopsy of adrenal masses: immediate and delayed complications," Journal of computer assisted tomography, vol. 19, pp. 434-439, 1995.

[12] P. Thampanitchawong and T. Piratvisuth, "Liver biopsy: complications and risk factors," World journal of gastroenterology, vol. 5, p. 301, 1999.

[13] C. I. R. S. Inc. (2013). Image-Guided Abdominal Biopsy Phantom.

[14] Plus toolkit - printable 3D models catalog.

[15] T. Allen, H. Krzywicki, and J. Roberts, "Density, fat, water and solids in freshly isolated tissues," Journal of applied physiology, vol. 14, pp. 1005-1008, 1959.

[16] N. D. Inc. (2013). Aurora Electromagnetic Tracking System.

CHAPTER 5

CARDIOVASCULAR CATHETER WITH AN EXPANDABLE ORIGAMI STRUCTURE

Radiofrequency Ablation for Atrial Fibrillation

Atrial fibrillation (AF) is a heart rhythm disorder characterized by rapid or irregular electrical activity in the atria. The atrial electrical signals bombard the atrioventricular (AV) node, allowing some signals to pass through the AV node to the ventricles, producing a rapid, irregular heart rate and often causing symptoms of palpitations, shortness of breath, or fatigue [1]. Over 750,000 people are hospitalized each year as a result of AF, and the condition contributes to an estimated 130,000 deaths each year [2]. These numbers are expected to rise as the average age of the U.S. population increases [3, 4].

Electrophysiology (EP) therapy is rapidly growing as a means for diagnosis and treatment of cardiac rhythm disorders. During treatment of AF, a specialized mapping/ablation catheter is inserted through the femoral artery (FA) and guided to the source of arrhythmia in the heart [5]. The catheter is then used to measure electrical voltages at various locations throughout the chambers of the heart. The collected information is used to create a spatial voltage distribution for locating the abnormal tissue causing the arrhythmia [6]. The abnormal tissue is then electrically inactivated through the transmission of radiofrequency energy [7]. This method, known as radiofrequency ablation (RFA), can restore the patient's regular heart rhythm. Both the RFA treatment

phase and the mapping diagnostic phase of EP procedures are heavily dependent on the electrophysiologist's ability to navigate the catheter to the intended location.

This chapter presents a novel expandable structure allowing for potential imaging and treatment electronics to be mounted to a catheter-based device. The origami folding method and a mathematical model are presented to demonstrate the ability to manufacture an expandable origami structure to suit specific patient anatomy and clinical instruments. A prototype of the expandable origami structure was scanned inside an MRI scanner to demonstrate the MRI compatibility of the design.

Device Design

Geometry/Mathematical Model

An optimal shape design for the origami structure was determined by evaluating the geometry and the available space for storing electronics. Nomenclature is shown in Table 5.1 for the below equations and symbols. The structure is a square grid comprised of *n* x *n* smaller individual squares (8 x 8 in the prototype displayed in Fig. 5.1). The height, *h*, of the fully stowed configuration is limited by the (1a) is given by

$$h = \frac{d}{n} \tag{1}$$

where *d* is the diameter of the fully expanded configuration (Fig. 5.1d) and *n* is the number of folds across the horizontal or vertical direction. The maximum allowable height of the stowed configuration is considered because the structure could get stuck in the aortic arch if the height is too large. Fig. 5.2a shows an MR image of the aortic arch with an overlaid image of the stowed origami structure as it passes through the aortic arch. The area, A_s, of the fully stowed configuration (perpendicular to the axis of the catheter) can be determined by

$$A_s = (h + t * 4n)^2 \quad (2)$$

where *t* is the material thickness. The diameter of the FA limits the maximum allowable stowed area. The surface area, A_e, of the fully expanded configuration is

$$A_e = \left(\frac{\pi}{4}\right) d^2 \quad (3)$$

The diameter of the left atrium (LA) limits the maximum allowable expanded surface area. Fig. 5.2b highlights the areas in the FA and LA where the origami structure will be stowed and expanded. The expanded surface area to stowed area ratio, R_a, is defined by

$$R_a = \frac{A_e}{A_s} \quad (4)$$

It is necessary for this ratio to be as large as possible to optimize the shape of the flasher and obtain the maximum achievable SNR.

Table 5.1. Symbol Nomenclature for Origami Structure Equations	
h	Height of the fully stowed configuration
d	Diameter of the fully expanded configuration
n	Number of folds across the horizontal or vertical direction
A_s	Area of the fully stowed configuration (perpendicular to catheter axis)
A_e	Surface area of the fully expanded configuration
t	Thickness of material
R_a	Expanded surface area to stowed area ratio
f	Frequency
Q	Quality factor
L	Inductance
C	Capacitance
R	Resistance
SNR	Signal to noise ratio
P_{center}	Mean signal of a 40 x 40 pixel region at the center of the phantom image
SD_{corner}	Standard deviation of the signal of a 40 x 40 pixel region at the corner of the image

(a) 0% expanded

(b) 30% expanded

(c) 70% expanded

(d) 100% expanded

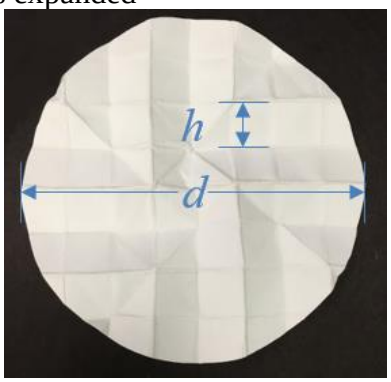

Figure 5.1. Origami structure expansion.

(a) MR image showing the aortic arch with the stowed origami structure overlaid

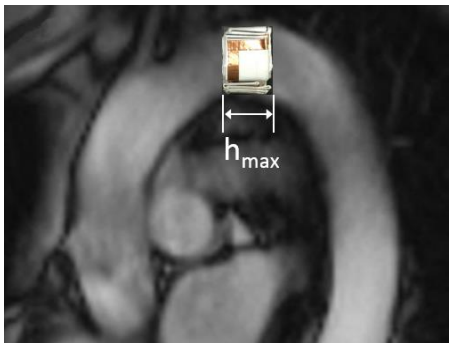

(b) MR images highlighting the area constraints of the origami structure. The blue highlights the area of the left atrium, where the catheter will be expanded, and the red highlights the area of the femoral artery, where the catheter will be stowed.

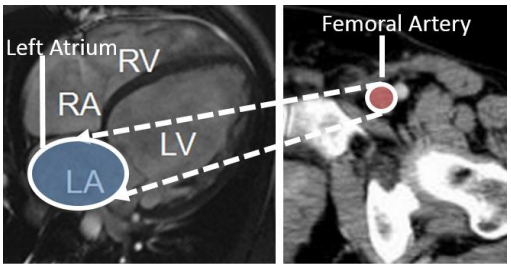

Blue: Area where flasher is expanded
Red: Area where flasher is stowed

Figure 5.2. Anatomy that the origami structure interacts with.

Mechanical Fabrication

The expandable origami structure was fabricated by folding a 40 mm x 40 mm sheet of biocompatible polycaprolactone into an iso-area flasher origami pattern [8] (Fig. 5.3). The material properties of the expandable structure allow it to be flexible enough to fold down to fit inside the body vasculature, yet stiff enough to expand once inside the heart chamber. After the structure has been deployed inside the heart and has captured the images, it is pulled out of the heart while still in the expanded configuration. The structure collapses on itself in the process, rendering it unusable for future imaging.

Once the base of the structure was assembled, a coil of 5 mm width copper was applied near the edge of the apparatus to form a receiver coil (Fig. 5.4a). Figures 5.4b, 5.4c, and 5.4d show prototypes of expandable structures containing 2, 4, and 8 imaging coils, respectively, to illustrate the potential for parallel imaging using this structure. This simple fabrication method allows for ease of prototyping as well as a straightforward proof of concept.

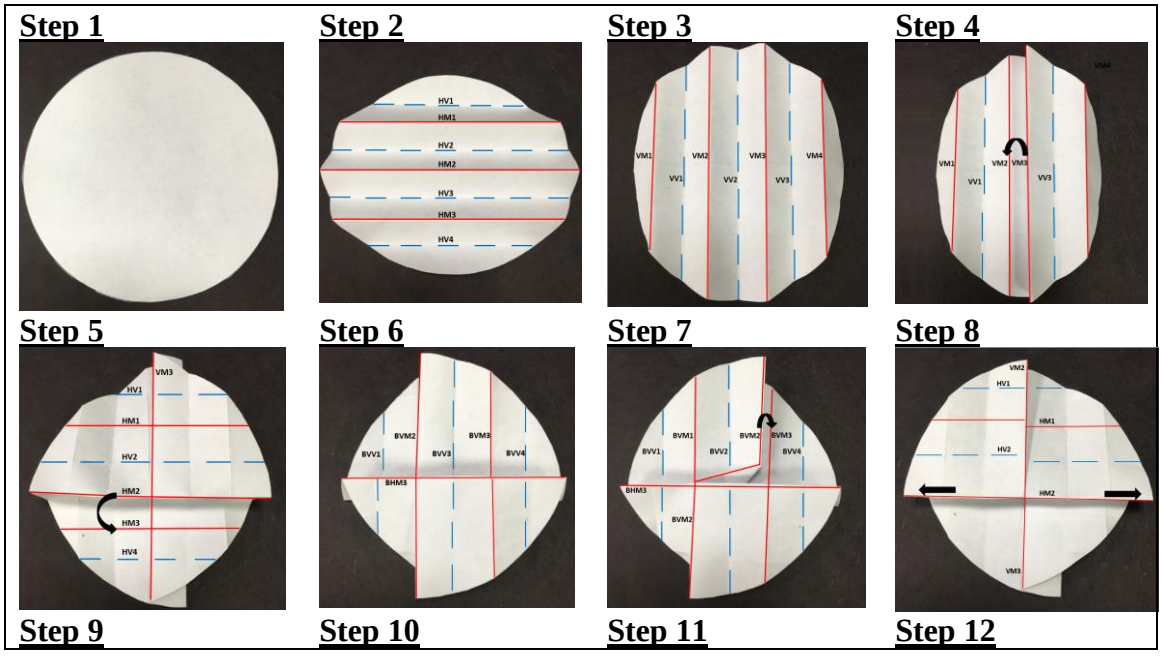

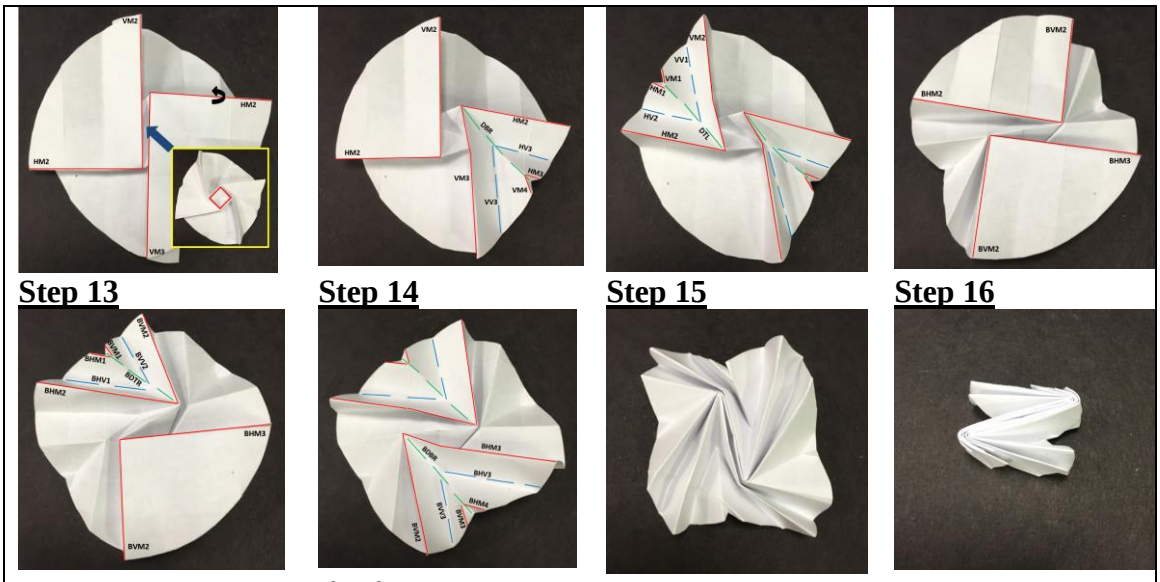

Figure 5.3. Instructions for folding expandable origami structure. **Step 1:** Cut out a circular sheet of paper. **Step 2:** Fold the 4 horizontal valley (HV) folds and the 3 horizontal mountain (HM) folds. **Step 3:** With the same sheet of paper and in the same orientation, fold the 4 vertical mountain (VM) folds and the 3 vertical valley (VV) folds. **Step 4:** Fold VM3 to VM2. **Step 5:** Fold HM2 down to HM3. **Step 6**: Turn over to bottom side. **Step 7**: Fold top half of back vertical mountain 2 (BVM2) to back vertical mountain 3 (BVM3). **Step 8**: Turn over to top side and pull left and right halves of HM2 apart until top layers separate from underlying layer. **Step 9**: Fold right half of HM2 to HM1. This should form a central square under the first layer of folds (illustrated in yellow box). **Step 10**: Fold HM2 to VM3 and fold HM3 and VM4 together between them, forming the diagonal bottom right (DBR) fold. **Step 11**: Fold HM2 to VM2 and fold HM1 and VM1 together between them, forming the diagonal top left (DTL) fold. **Step 12**: Turn over. **Step 13**: Fold BHM2 to BVM2 and fold BHM1 and BVM1 together between them, forming BDTL. **Step 14**: Fold BHM3 to BVM2 and fold BHM4 and BVM3 together between them, forming BDBR. **Step 15**: Push the outside corners together and keep orientation of previous folds. **Step 16**: Continue pushing corners together until top and bottom edges come together.

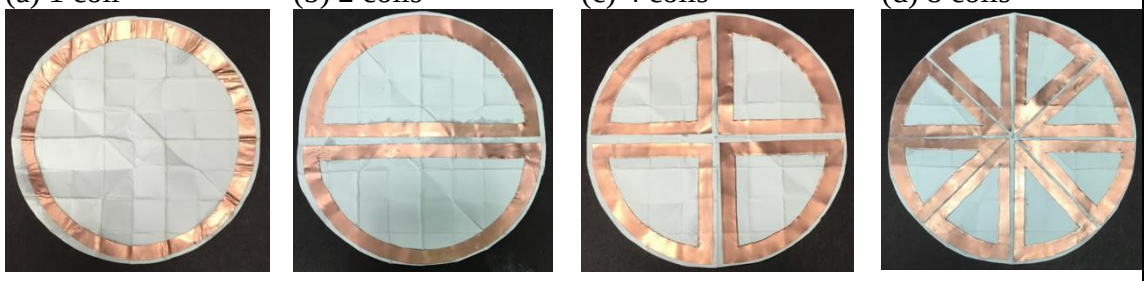

Figure 5.4. Origami structure containing varying numbers of imaging coils.

Tuning and Matching Electronics

The imaging coil was connected to a tuning-matching circuit (Fig. 5.5a) sealed in a box at the proximal end of the stylet through a micro-coaxial cable [9, 10]. The circuit was tuned and matched based on a single coil topology to prove the concept of the origami structure incorporated with imaging electronics. A network analyzer was then used to tune the embedded circuit to 128 MHz (3T Larmor frequency) and used to match the circuit to the universal standard of 50-ohm resistance (Fig. 5.5b).

(a) Circuit diagram of the tuning-matching circuit. The circuit was tuned based on a single coil topology to prove the concept of the origami structure incorporated with imaging electronics.

(b) Network analysis displaying the reflection efficiency of the coil resonance frequency tuned to 128 MHz for 3T Larmor frequency

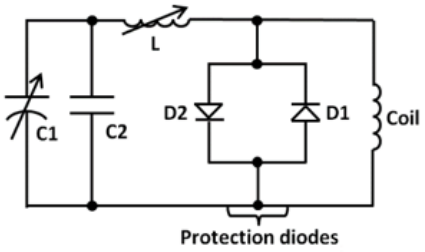

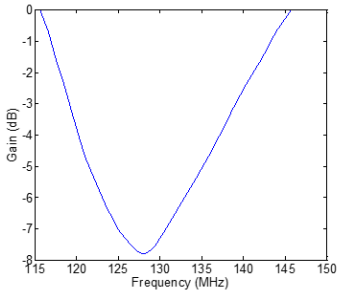

Figure 5.5. Tuning-matching circuit tuned to the Larmor Frequency.

The second order RLC circuit consists of a resistor that consumes energy and induces a damping effect during the resonance. The energy is stored in the capacitor and inductor, both of which determine the resonance frequency of the circuit. Referring to [11], the resonance frequency of the system can be written as

$$f = \frac{1}{2\pi\sqrt{LC}} \tag{5}$$

where L and C are the inductance and capacitance of the circuit respectively. From Eq. (5) alone, there are infinite combinations of the L and C to generate a specific resonance

value. However, it is worth noting the quality factor, acting as another important consideration of designing the RLC circuit, which can be written as

$$Q = \frac{1}{R}\sqrt{\frac{L}{C}} \tag{6}$$

A larger *Q* value correlates to a larger amount of magnetic energy that can be stored by the micro coil. Therefore, a trade-off between *L* and *C* need to be made in the tuning-matching of the coil. The quality factor of the imaging coil circuit was calculated to be 8.533.

MRI Compatibility Test

An MR image that has been negatively affected by the presence of a non-compatible device or object has a lower SNR. Certain devices or objects may not cause artifact disturbances due to either being solely constructed of compatible materials or by a large physical separation. Active devices (which contain electrically powered components or are otherwise capable of producing electromagnetic (EM) field emissions) can cause SNR reduction if their emitted fields are picked up by the scanner receive coil. To evaluate the effect on MR image SNR of the system and the effect of the shielding, every active component of the system intended to be used within the scanner room was tested independently before the system was tested.

The implemented test method was adapted from the protocol put forward by Chinzei [12] for electrical and electronic components. According to the standard defined by Chinzei, the acceptable level of SNR reduction is up to 10 %. However, this value is intended as a guideline rather than a strict qualifier of compatibility. In practice, the acceptable level of SNR reduction is dependent on the intended method of application. A

very low degree may be required for the determination of soft tissue boundaries from an image, but a much less stringent requirement may be necessary for image guided gross positioning of instruments.

The implemented test method was conducted as follows:

1. A container was filled with CuSO4 solution (1.25 g/l concentration) and scanned with a spin echo and a gradient echo sequence; these images were used as the control image. The image sequence parameters must be maintained constant throughout the duration of the subsequent testing.
2. The origami structure was placed next to the phantom without power connected and the phantom was scanned with the same scan sequence combination.
3. In the same configuration, a further scan was taken with the origami structure closed and connected to the scanner.
4. In the same configuration, a further scan was taken with the origami structure expanded and connected to the scanner.
5. DICOM format images were produced. The SNR of an image is calculated using Equation 7, where P_{center} is the mean signal of a 40 x 40-pixel region at the center of the phantom image and SD_{corner} is the standard deviation of the signal of a 40 x 40-pixel region at the corner of the image. The variation of SNR is calculated by subtracting the SNR value of the corresponding control image.

$$SNR = \frac{P_{center}}{SD_{corner}} \tag{7}$$

The method requires the origami structure in the bore to be connected to the scanner with the flasher actuated at different stages (e.g. stowed, expanded). As such, the

full system including the auxiliary tuning and matching electronic hardware must be included in the scanner room during the test.

Device Analysis and Evaluation

Geometry/Mathematical Model

The geometric evaluation of the expandable origami structure was used to create a mathematical model for determining the optimal dimensions of the structure. Fig. 5.6 shows plots displaying the relationship of height (Fig. 5.6a), stowed area (Fig. 5.6b), and expanded surface area (Fig. 5.6c) to the expanded diameter and the number of folds. Using these plots, the ideal shape of the expandable structure based on the curvature of the aortic arch, the inner diameter of the guide catheter, and the diameter of the LA can be defined. The average diameter of the FA at the hip is approximately 8.2 ± 0.14 mm [13]. The average diameter of the LA is approximately 27 – 38 mm in women and 30 – 40 mm in men [14]. Using this data, appropriate values for the height h, the stowed area A_s, and the expanded area A_e can be found using equations 1, 2, and 3. h is calculated from equation 1 to be 4.25 mm using an estimated diameter d matching that of the 34 mm average diameter of the LA in humans [14] and using $n = 8$ as in the prototype shown in this report. A_s is calculated via equation 2 to be an estimated 196 mm^2 using a material thickness t of 0.25 mm. A_e is calculated via equation 3 to be approximately 1120 mm^2. The expanded surface area to stowed area ratio R_a is therefore estimated to be 5.71 using equation 4 (Table 5.2).

(a) Stowed height (b) Stowed area (c) Expanded surface

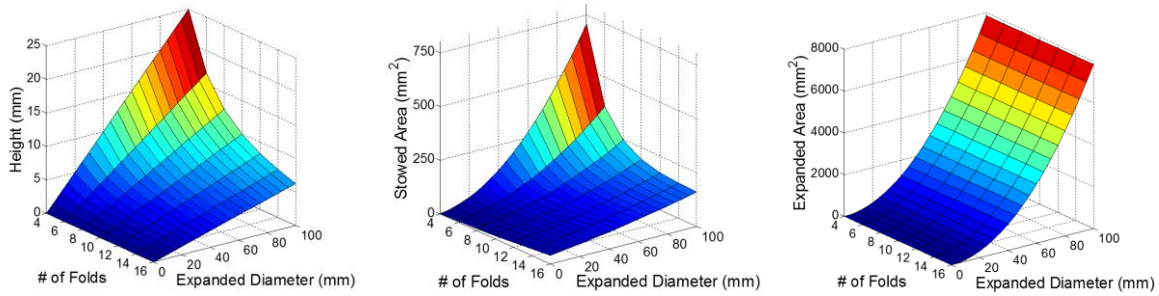

Figure 5.6. Plots displaying (a) stowed height, (b) stowed area, and (c) expanded surface area against expanded diameter and the number of folds contained across the width of the structure.

Table 5.2. Origami Structure vs Mechanical Constraint Case Study

Structure Dimension	**Mechanical Constraint**	**Calculated Value**	**Equation Used**
H (Height)	Aortic arch curvature	4.25 mm	1
A_s (Stowed Area)	FA inner diameter	196 mm^2	2
A_e (Expanded Area)	LA inner diameter	1120 mm^2	3
R_a (Area Ratio)	FA and LA inner diameters	5.71	4

MRI Compatibility Test

The SNR reduction of the expandable origami structure was examined. The experiment was conducted in a 3T Siemens MRI scanner. The results are shown in Fig. 5.7. The maximum SNR reduction in the origami catheter was 0.54% with the turbo spin echo (TSE) sequence, and 0.46% with the True fast imaging with steady-state free precession (True FISP) sequence. Even though the SNR reduction varies in different scan conditions, they are all within the acceptable level of 10% proposed by Chinzei [12], showing good compatibility of the individual components. This experiment demonstrates

the usability of the expandable origami structure with its individual electronic components in the MR environment.

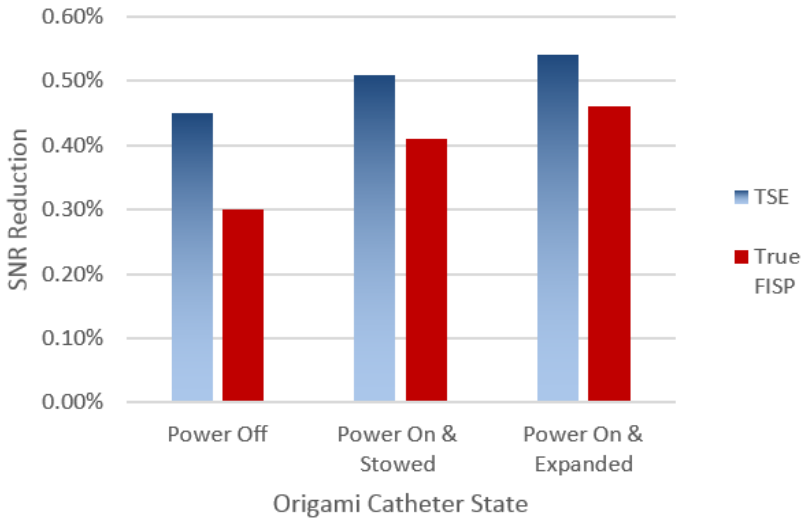

Figure 5.7. Results from SNR reduction experiment. Image sequence parameters: TSE – TR/3600ms, TE/120ms, Flip Angle/180 degrees, number of slice/5mm, spacing/5mm, resolution/256X256, Field of View (FOV)/300mm, Band Width/130Hz/px; True FISP – TR/22ms, TE/10ms, Flip Angle/30 degrees, number of slice/5mm, spacing/5mm, resolution/256X256, Field of View (FOV)/300mm, Band Width/130Hz/px.

Discussion

Treatment of cardiac arrhythmia through catheter ablation can permanently resolve the condition and significantly improve patients' quality of life. The expandable origami structure for storing MRI imaging coils on the tip of a catheter offers an improved method for treatment of cardiac arrhythmia, but further studies are required to validate the safety and the capabilities of the structure. The expandable structure must be able to integrate with the catheter through either some effective means of attachment or through direct fabrication of the two parts as one. In vivo animal trials and human pilot studies must be conducted to confirm the devices ability to safely deploy inside the LA and safely retract from the body. The shape of the structure will be compared to other

potential shapes to determine the safest structure. For example, a voluminous structure could potentially offer more safety as opposed to a flat structure because it would not contain sharp edges. Further MRI scans must be performed to validate the devices ability to perform real time cardiac imaging.

This chapter presents the design of a novel expandable origami mechanism that aims to assist in diagnostic and therapeutic stages of EP treatments. The expandable structure was developed by folding a thin sheet of biocompatible polycaprolactone into an iso-area flasher and the embedded electrical circuit was constructed by applying imaging coils around the structure. The circuit was tuned and matched via network analysis to the Larmor frequency of a 3T MRI at 128 MHz. Equations relating expanded surface area and stowed area were derived from basic geometry to optimize the shape of the flasher based on patient anatomy. SNR reduction results demonstrate that the imaging coil is MRI compatible. Future experiments performing actual cardiac imaging are required to validate the efficacy of the device.

References

[1] A. Ames and W. G. Stevenson, "Catheter ablation of atrial fibrillation," *Circulation,* vol. 113, pp. e666-e668, 2006.

[2] Center for Disease Control. (2015). *Atrial Fibrillation.* Available: http://www.cdc.gov/dhdsp/data_statistics/fact_sheets/fs_atrial_fibrillation.htm

[3] Y. Miyasaka, M. E. Barnes, B. J. Gersh, S. S. Cha, K. R. Bailey, W. P. Abhayaratna, J. B. Seward, and T. S. M. Tsang, "Secular trends in incidence of atrial fibrillation in Olmsted County, Minnesota, 1980 to 2000, and implications

on the projections for future prevalence," *Circulation,* vol. 114, pp. 119-125, 2006.

[4] P. A. Wolf, E. J. Benhamin, A. J. Belanger, W. B. Kannel, D. Levy, and R. B. D'Agostino, "Secular trends in the prevalence of atrial fibrillation: The Framingham Study," *American heart journal,* vol. 131, pp. 790-795, 1996.

[5] M. G. Glowny and F. S. Resnic, "What to Expect During Cardiac Catheterization," *Circulation,* vol. 125, pp. e363-e364, 2012.

[6] C. Knackstedt, P. Schauerte, and P. Kirchhof, "Electro-anatomic mapping systems in arrhythmias," *Europace,* vol. 10, pp. iii28-iii34, 2008.

[7] A. J. Wood and F. Morady, "Radio-frequency ablation as treatment for cardiac arrhythmias," *New England Journal of Medicine,* vol. 340, pp. 534-544, 1999.

[8] J. Shafer, *Origami to Astonish and Amuse*: St. Martin's Press, 2001.

[9] Y. Chen, W. Wang, E. Schmidt, K.-W. Kwok, A. Viswanathan, R. Cormack, and Z. T. H. Tse, "Design and Fabrication of MR-Tracked Metallic Stylet for Gynecologic Brachytherapy."

[10] W. Wang, A. N. Viswanathan, A. L. Damato, Y. Chen, Z. Tse, L. Pan, J. Tokuda, R. T. Seethamraju, C. L. Dumoulin, E. J. Schmidt, and R. A. Cormack, "Evaluation of an active magnetic resonance tracking system for interstitial brachytherapy," *Medical physics,* vol. 42, pp. 7114-7121, 2015.

[11] R. P. Feynman, R. B. Leighton, and M. Sands, *The Feynman Lectures on Physics*: Reading, MA: Addison-Wesley Longman, 1964.

[12] K. Chinzei, R. Kikinis, and F. A. Jolesz, "MR compatibility of mechatronic devices: design criteria," in *Medical Image Computing and Computer-Assisted Intervention–MICCAI'99*, 1999, pp. 1020-1030.

[13] S. Crisan, "Ultrasound examination of the femoral and popliteal arteries," *Medical ultrasonography*, vol. 14, p. 74, 2012.

[14] R. M. Lang, M. Bierig, R. B. Devereux, F. A. Flachskampf, E. Foster, P. A. Pellikka, M. H. Picard, M. J. Roman, J. Seward, J. Shanewise, S. Solomon, K. T. Spencer, M. St. J. Sutton, and W. Stewart, "Recommendations for chamber quantification," *European Heart Journal-Cardiovascular Imaging*, vol. 7, pp. 79-108, 2006.

CHAPTER 6

MR CONDITIONAL SMA-BASED ORIGAMI JOINT

Minimally Invasive Surgery with Magnetic Resonance Imaging

Minimally invasive surgery (MIS) has quickly become one of the most promising fields for surgical procedures. The goal of MIS is to minimize incisions to reduce postoperative pain and blood loss, speed recovery, and lessen scarring [1, 2]. MIS procedures have been enabled by the advance of microfabrication of various medical devices. However, a major drawback to this technique is the increased costs due to investment in the equipment required and the use of disposable instruments [3]. The cost of disposable MIS devices can be significantly reduced through simplification of fabrication techniques. Origami provides distinct efficiency in creating three-dimensional geometry without assembly by folding a single sheet of material [4]. The implementation of origami structures into minimally invasive surgical instruments is a promising new field that has numerous applications [5-8]. Recently, there has been an emerging field using origami to create compliant mechanisms, which can provide alternative ways to develop joints that achieve a particular range of motion [9, 10]. Devices that can provide precise navigation through curved anatomical pathways are crucial during these types of surgery, which makes the dexterity of origami structures especially useful in MIS [11].

Magnetic resonance imaging (MRI) provides high contrast visualization of soft tissue, making it ideal for image-guided procedures. Currently, most MRI is diagnostic due to the inherent limitations present within a strong magnetic field. However, research

shows that MRI can be used for intraoperative procedures such as navigating catheters in cardiovascular interventions [12]. The American Society for Testing and Materials (ASTM) standard F2503-13 [13] classifies devices for the MR environment. MR conditional items are those that have been demonstrated to pose no known hazards in a specified MRI environment.

In this study, a chain of compliant rolling-contact element joints [14] was designed. The origami joints were derived from curved-folding origami techniques that enable the capability of being assembled from a single sheet of material. Many traditional endoscopes contain a series of pin joints for manipulation [15]. The origami joints used in this study aimed to reduce the complications that arise in pin joints such as backlash and wear. The origami joints can be completely assembled from a single sheet of material, greatly reducing the cost of fabrication by eliminating assembly of various components.

The origami joints were actuated using shape-memory alloy (SMA). SMA is an alloy that can recover an apparent permanent strain once heated to its activation temperature [16]. SMA is in the martensite phase at lower temperatures and can be easily deformed. When the SMA is heated, it returns to its pre-deformed shape set at the austenite phase [17]. Previous similar studies have shown to provide around 3 N of force using SMA [18]. Real-time active water cooling can be used with SMA to avoid tissue burning and to increase actuation bandwidth [19].

The geometry of the joint was analyzed to derive equations that define the location of the end-effector position. Mathematical software was used to model the resulting equations to visualize the physical range of the joint. The desired position of the end-effector could then be found by utilizing inverse kinematics.

The origami joint chain was introduced into the MRI environment to evaluate its MRI compatibility. The ability of the device to be MR conditional allows it to be used in MRI-guided surgical procedures, making it a valuable additional tool to assist surgeons in navigating anatomical pathways.

The novel contributions in this chapter include: 1) For the first time, a joint chain was developed based on origami principles and smart actuators, 2) the joint chain was low-cost and disposable as it was assembled from a single sheet of material, and 3) the joint chain was MR conditional.

Origami Joint Design

Origami Folding Plan of the Joint Chain

The flat printed folding pattern of a chain of four origami joints is presented in Fig. 6.1a. The design can be laser cut, significantly reducing fabrication time. Black lines represent where the structure is cut, and red lines represent where it is folded. The folding pattern of a single origami joint is shown in Fig. 6.1b. Two rolling surfaces are connected by flexible bands, which forms a functional joint (Fig. 6.1c). A link connects each joint with an orientation of 90 degrees to the next adjacent joint, which provides for multiple degrees of freedom. The joint and link structures were designed so that a lumen is available for a catheter or other instruments to go through the joint chain. The position of the structure can be modeled using forward kinematic equations.

(a) Folding pattern of an origami chain of four joints

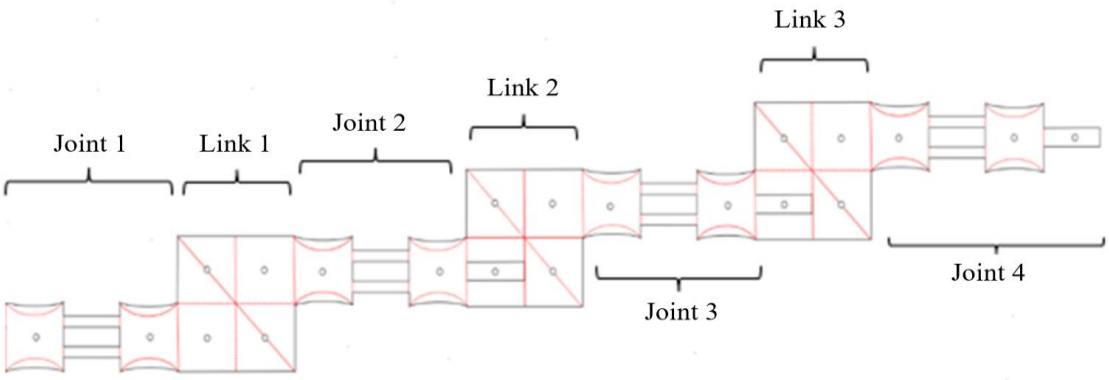

(b) Folding pattern for a single origami joint

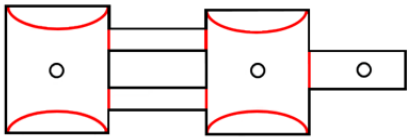

(c) Final folded form of a single origami joint [14]

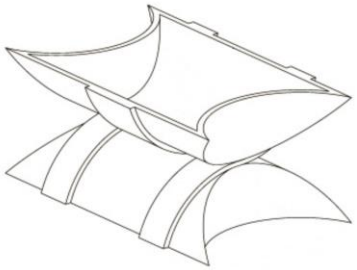

Figure 6.1. Origami joint folding pattern.

Kinematic Model for Planar Origami Joint

The kinematics of the origami joint were used to describe the joint chain's end effector position in relation to the angle of deflection of each joint. A mathematical model was derived by building up from a single joint to a chain of *n* joints (Fig. 6.2).

The point of contact between the two halves of a single origami joint with relation to its deflection angle was determined from the total deflection θ of the joint and the radius of the cam R (Fig. 6.2a). Nelson et al [14] determined that the structure of the origami joint is modelled by a cylindrical cam. The equation of the length L of a single panel is shown by

$$L = 2R \sin\frac{\theta}{2} \tag{1}$$

Using the Pythagorean Theorem,

$$R^2 = D^2 + \left(\frac{L}{2}\right)^2 \tag{2}$$

Substituting for L and rearranging,

$$D = R\sqrt{1 - \left(\sin\frac{\theta}{2}\right)^2} \tag{3}$$

D was then be used to determine the relationship between the angle of rotation of the joint, α, and the (x, y) coordinates of the point of contact between the two rolling elements in the origami joint (Fig. 6.2b). From Fig. 6.2 and the law of sines,

$$\frac{\sin(90+\alpha)}{R} = \frac{\cos\alpha}{R} = \frac{\sin\beta}{D} \tag{4}$$

Solving for β and substituting for β,

$$\beta = \sin^{-1}\left(\frac{D}{R}\cos\alpha\right) \tag{5}$$

$$c + (90 + \alpha) + \sin^{-1}\left(\frac{D}{R}\cos\alpha\right) = 180 \tag{6}$$

Solving for c,

$$c = 90 - \alpha - \sin^{-1}\left(\frac{D}{R}\cos\alpha\right) \tag{7}$$

Then using the law of sines again,

$$r = \frac{R\sin c}{\cos\alpha} = \frac{R\sin 90-\alpha-\sin^{-1}\left(\frac{D}{R}\cos\alpha\right)}{\cos\alpha} \tag{8}$$

Substituting for D,

$$r = \frac{R\sin 90-\alpha-\sin^{-1}\left(\sqrt{1-\left(\sin\frac{\theta}{2}\right)^2}\cos\alpha\right)}{\cos\alpha} \tag{9}$$

Let γ be the numerator of r.

$$\gamma = R\sin 90 - \alpha - \sin^{-1}\left(\sqrt{1 - \left(\sin\frac{\theta}{2}\right)^2}\cos\alpha\right) \tag{10}$$

r can be expressed as

$$r = \frac{\gamma}{\cos \alpha} \tag{11}$$

x and *y* are found in terms of *r* by

$$x = r \cos \alpha \tag{12}$$

$$y = r \sin \alpha \tag{13}$$

Thus, when given the coordinates to the origin of the origami joint (x_o, y_o), one can find the coordinates (x, y) of the point of contact of the joint. Take, for example, Fig. 6.2c, which shows the geometry of a chain of two origami joints in a two-dimensional plane (a structure with one degree of freedom). The coordinates of the points of contact between each joint, (x_n, y_n) can be determined by finding the origin coordinates (x_{o_n}, y_{o_n}) and adding the results from (12) and (13). Assuming the first origin coordinates are $(0, 0)$ the next origin coordinates for the next joint in the chain is determined by

$$x_{o_2} = x_1 + t_1 \cos \alpha_1 \tag{14}$$

$$y_{o_2} = y_1 + r_1 + t_1 \sin \alpha_1 \tag{15}$$

Where *t* is the thickness of each link (Fig. 6.2c). The point of contact of the second joint is at

$$x_2 = x_{o_2} + r_2 \cos(-90 + \alpha_1 + \alpha_2) \tag{16}$$

$$y_2 = y_{o_2} + r_2 \sin(-90 + \alpha_1 + \alpha_2) \tag{17}$$

For *n* joints, the point of contact of the *n*-th joint is at

$$x_n = \sum_{i=1}^{n}\left[\frac{\gamma_i}{\cos\alpha_i}\cos\left((i-1)\left(-\frac{\pi}{2}\right)+\sum_{j=1}^{i}\alpha_j\right)\right] + \sum_{i=1}^{n-1}\left[t_i\cos\left((i-1)\left(-\frac{\pi}{2}\right)+\sum_{j=1}^{i}\alpha_j\right)\right] + \sum_{i=2}^{n-1}\left[\frac{\gamma_i}{\cos\alpha_i}\cos\left((i-2)\left(-\frac{\pi}{2}\right)+\sum_{j=1}^{i-1}\alpha_j\right)\right] \quad (18)$$

$$y_n = \sum_{i=1}^{n}\left[\frac{\gamma_i}{\cos\alpha_i}\sin\left((i-1)\left(-\frac{\pi}{2}\right)+\sum_{j=1}^{i}\alpha_j\right)\right] + \frac{\gamma_1}{\cos\alpha_1} + \sum_{i=1}^{n-1}\left[t_i\sin\left((i-1)\left(-\frac{\pi}{2}\right)+\sum_{j=1}^{i}\alpha_j\right)\right] + \sum_{i=2}^{n-1}\left[\frac{\gamma_i}{\cos\alpha_i}\sin\left((i-2)\left(-\frac{\pi}{2}\right)+\sum_{j=1}^{i-1}\alpha_j\right)\right] \quad (19)$$

(a) Origami joint cam

(b) Geometry to determine D from the angle of rotation of the origami joint

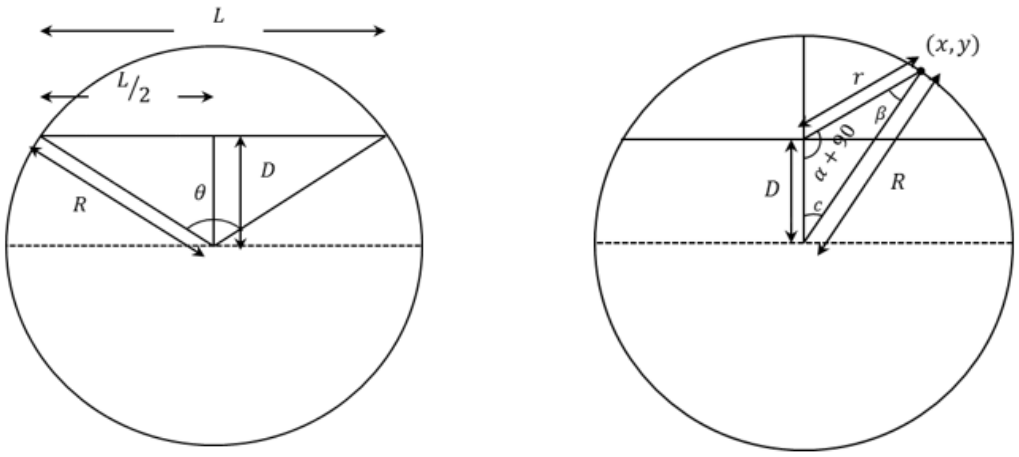

(c) 2-D geometric representation of the rotation in space of a chain of origami joints

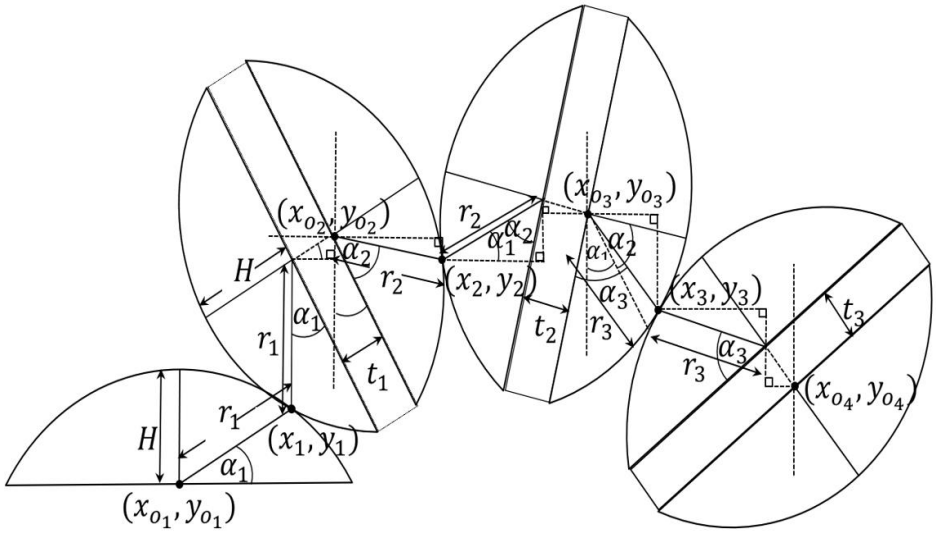

Figure 6.2. Geometric analysis of the origami joint structure.

Shape Memory Alloy Actuation

The origami joints were actuated with shape-memory alloy (SMA) springs made of nitinol wire. The SMA springs were conditioned so that when heat is applied, they return to their tightly wound memory shape. Each joint contained two SMA springs: one on both the right and left sides. When an electrical current is applied to one of the SMA

springs, it returns to its memory shape, which causes the other spring to stretch (Fig. 6.3a). This effectively actuates the joint in one direction. The direction of actuation of the joint was regulated by controlling the current applied to each spring. The size of the origami joint prototype shown in Fig. 6.3b was approximately 12 mm x 12 mm x 12 mm and the cost is less than one US dollar.

(a) Progression of actuation of a two origami joints from 0° - 20°

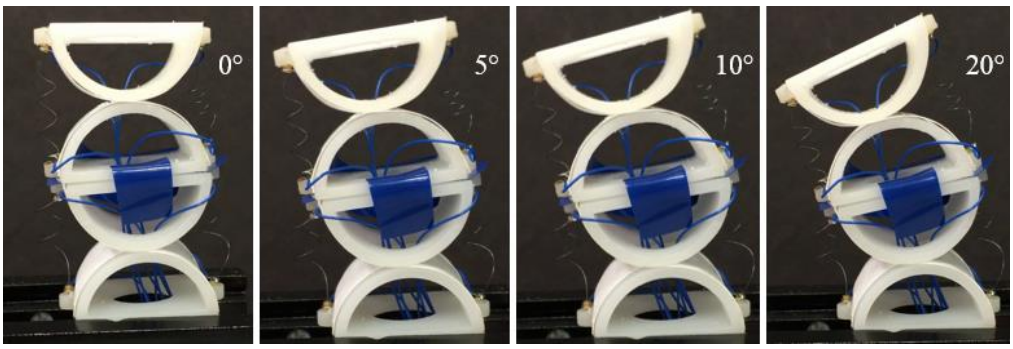

(b) Size comparison of an origami joint prototype to a human pinky

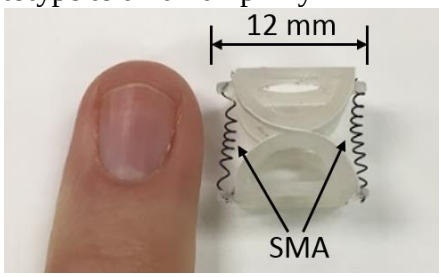

(c) CAD model of origami joint chain

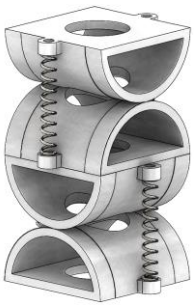

Figure 6.3. Origami joint prototypes and CAD model.

Electronic Circuitry

Each origami joint was connected to four cables that provide electricity to actuate the two springs. The cables were fed through the central lumen of the device. An open-loop control circuit was developed based on H-bridge electronics and pulse width modulation (PWM) to regulate the input current to achieve a desired bending angle output.

Origami Joint SMA Performance Analysis

The performance of the SMA was analyzed through experiments which compared current vs bending angle, current vs temperature, current vs force, and response time vs angle at various currents. Upon loading and unloading the SMA with current, hysteresis was observed and recorded. The force generated was measured by actuating the joint with weights hanging from one side of the structure. As more current was applied, more weight could be lifted. The actuation angle was measured using a protractor, and the SMA temperature was measured using a temperature probe.

Origami Joint Material Properties

The prototype in Fig. 6.3 was constructed by folding the origami pattern in Fig. 6.1 from cardstock and further strengthened by inserting a photopolymer. The mechanical properties of the photopolymer are given in Table 1.

Table 6.1. Photopolymer Properties		
Mechanical Properties	Measurement	Method
Ultimate Tensile Strength	38 MPA	ASTM D 638-10
Young's Modulus	1.6 Gpa	ASTM D 638-10
Elongation at Failure	12%	ASTM D 638-10
Flexural Modulus	1.25 Gpa	ASTM C 790-10
Thickness	1 mm	n/a

Origami Joint Performance Evaluation

Origami Joint SMA Performance Results

The performance results of the SMA are shown in Fig. 6.4. The results show that the degree of bending was approximately ±9 degrees per joint with the current limited to 1.5 A. The SMA reached a temperature of approximately 150 degrees Celsius at a current

of 1.25 A. The joint had a response time of < 4 seconds and an actuation force of 0.5 N with 1.25-A current. The results of the observed hysteresis of the SMA upon loading and unloading of current is shown in Fig. 6.4e. The results indicate that the bending angle, actuation force and SMA temperature had a predictable response curve with respect to the applied current, making the origami chain feasible for use in endoscopic applications with future improvements.

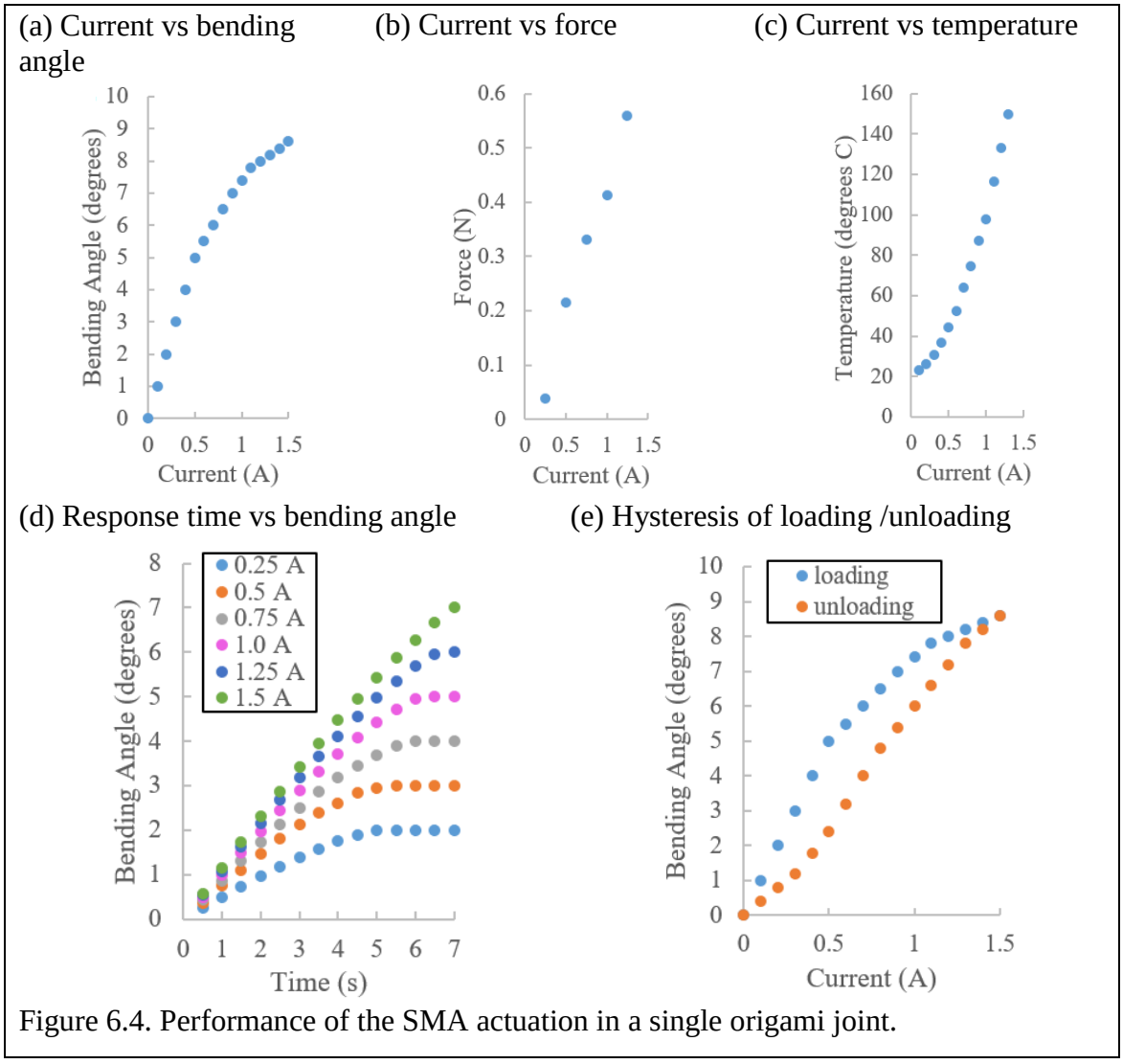

Figure 6.4. Performance of the SMA actuation in a single origami joint.

MRI Compatibility Evaluation

The origami joint was tested using a 3T MRI scanner according to ASTM F2503-13 [13]. The scientific rationale was first employed based on the component materials of the joint. The joint was then tested for the static magnetic field-induced displacement force (ASTM F2052) and torque (ASTM F2213) by suspending the manipulator at the entrance of the MR system bore by a string and measuring the string deflection angle and observing the torque. The RF field-induced heating (ASTM F2182, ISO TS 10974) and gradient field-induced heating and vibration (ISO 10974) were performed by direct observation. The gradient and RF field-induced voltage tests (ISO TS 10974) were also performed by direct observation. By these experiments, the origami joint was validated as MR conditional in a 3T environment. MR images were taken of the prototype and the results showed a minimal artifact size of <1 mm measured from the boundary of the joint (Fig. 6.5a). The signal-to-noise ratio (SNR) reduction was measured by comparing a baseline measurement with no device present to measurements with the device present at power levels of 0%, 25%, 50%, 75%, and 100% using gradient echo (GE) and spin echo (SE) sequences. The results provided in Fig. 6.5d show a SNR reduction of less than 10%.

(a) MRI images of an origami joint chain

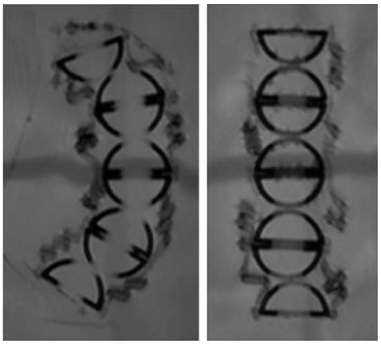

(b) Photo of the control box inside the MRI scanner

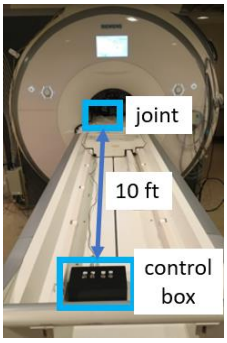

(c) Block diagram displaying the control of the joint chain inside the MRI

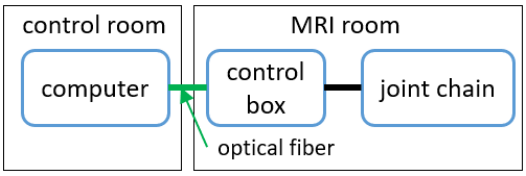

(d) SNR reduction of gradient echo (GE) and spin echo (SE) sequences

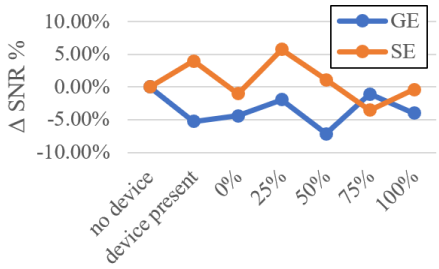

Figure 6.5. Origami joint chain MRI analysis.

Discussion

MR conditional surgical devices provide a means for interventional procedures with the guidance of high-quality imaging. The structure of the MR conditional flexible SMA-based origami joint chain was fabricated from a single sheet of material, which makes it a low cost and disposable surgical instrument. The origami joints were actuated via SMA springs that were attached to the sides of the joints. There was a lumen integrated into the joints through which a camera, catheter, or some other surgical instrument can be threaded. The geometry of the structure was analyzed and a 2-D end-effector range plot was produced. The mechanical performance evaluation resulted in ±9 degrees of bending in the origami joint with just 1.5 A of current. The device was tested

according to the ASTM standards [13], and the resulting images exhibited minimal artifacts, verifying it as an MR conditional device. Future work includes experimenting with various materials to make the structure more rigid, performing horizontal loading and parasitic motion analyses, and further miniaturizing the design by approximately 50% to match industry standard endoscopes. This chapter presented a novel application of origami and SMA to produce an MR conditional joint that has potential applications in endoscopy.

References

[1] B. Jaffray, "Minimally invasive surgery," Archives of disease in childhood, vol. 90, no. 5, pp. 537-542, 2005.

[2] N. Zemiti, G. Morel, T. Ortmaier, and N. Bonnet, "Mechatronic design of a new robot for force control in minimally invasive surgery," IEEE/ASME Transactions On Mechatronics, vol. 12, no. 2, pp. 143-153, 2007.

[3] K. Fuchs, "Minimally invasive surgery," Endoscopy, vol. 34, no. 02, pp. 154-159, 2002.

[4] B. Edmondson, "Development of a Thickness Accommodation Technique for Origami-Inspired Design," 2015.

[5] M. Johnson et al., "Fabricating biomedical origami: a state-of-the-art review," International journal of computer assisted radiology and surgery, vol. 12, no. 11, pp. 2023-2032, 2017.

[6] A. J. Taylor, Y. Chen, M. Fok, A. Berman, K. Nilsson, and Z. T. H. Tse, "Cardiovascular Catheter With an Expandable Origami Structure," Journal of Medical Devices, vol. 11, no. 3, p. 034505, 2017.

[7] B. J. Edmondson, L. A. Bowen, C. L. Grames, S. P. Magleby, L. L. Howell, and T. C. Bateman, "Oriceps: Origami-inspired forceps," in ASME 2013 conference on smart materials, adaptive structures and intelligent systems, 2013, pp. V001T01A027-V001T01A027: American Society of Mechanical Engineers.

[8] M. Salerno, K. Zhang, A. Menciassi, and J. S. Dai, "A novel 4-DOFs origami enabled, SMA actuated, robotic end-effector for minimally invasive surgery," in Robotics and Automation (ICRA), 2014 IEEE International Conference on, 2014, pp. 2844-2849: IEEE.

[9] I. L. Delimont, S. P. Magleby, and L. L. Howell, "Evaluating compliant hinge geometries for origami-inspired mechanisms," Journal of Mechanisms and Robotics, vol. 7, no. 1, p. 011009, 2015.

[10] K. Francis, J. Blanch, S. Magleby, and L. Howell, "Origami-like creases in sheet materials for compliant mechanism design," Mechanical Sciences, vol. 4, no. 2, pp. 371-380, 2013.

[11] L. A. Bowen, W. Baxter, S. P. Magleby, and L. L. Howell, "A position analysis of coupled spherical mechanisms found in action origami," Mechanism and Machine Theory, vol. 77, pp. 13-24, 2014.

[12] S. R. Dukkipati et al., "Electroanatomic mapping of the left ventricle in a porcine model of chronic myocardial infarction with magnetic resonance–based catheter tracking," Circulation, vol. 118, no. 8, pp. 853-862, 2008.

[13] A. Standard, "F2503–13," Standard Practice for Marking Medical Devices and Other Items for Safety in the Magnetic Resonance Environment. ASTM International, 2013.

[14] T. G. Nelson, R. J. Lang, S. P. Magleby, and L. L. Howell, "Curved-folding-inspired deployable compliant rolling-contact element (D-CORE)," Mechanism and Machine Theory, vol. 96, pp. 225-238, 2016.

[15] A. Loeve, P. Breedveld, and J. Dankelman, "Scopes too flexible... and too stiff," IEEE pulse, vol. 1, no. 3, pp. 26-41, 2010.

[16] L. M. Schetky, "Shape-Memory Alloys," Kirk-Othmer Encyclopedia of Chemical Technology, 1982.

[17] Z. Wei, R. Sandstroröm, and S. Miyazaki, "Shape-memory materials and hybrid composites for smart systems: Part I Shape-memory materials," Journal of Materials Science, vol. 33, no. 15, pp. 3743-3762, 1998.

[18] M. Ho, Y. Kim, S. S. Cheng, R. Gullapalli, and J. P. Desai, "Design, development, and evaluation of an MRI-guided SMA spring-actuated neurosurgical robot," The International journal of robotics research, vol. 34, no. 8, pp. 1147-1163, 2015.

[19] S. S. Cheng, Y. Kim, and J. P. Desai, "New actuation mechanism for actively cooled SMA springs in a neurosurgical robot," IEEE Trans. Robot., vol. 33, no. 4, pp. 986-993, 2017.

CHAPTER 7

MODULAR FORCE-APPROXIMATING SOFT ROBOTIC PNUEMATIC ACTUATOR

Soft Robots

Endoscopes are widely used in diagnosis and treatment of human diseases to provide visualization of lesions within internal organs with high resolution [1, 2]. They can be inserted through natural body orifices to access internal organs, rather than through incision [3]. Both illumination and detection elements must be navigated through difficult anatomical pathways, requiring a combination of flexibility and stiffness [4]. A high degree of stiffness can lead to dangerous complications such as perforation of soft tissue or organs [5]. There is enormous potential for research to improve the safety of instruments used to travel along complicated trajectories through the human anatomy. Soft robots offer a unique solution due to their inherent compliance and various actuation methods.

Soft robots have made a significant impact in the field of medical devices in applications ranging from wearable tactile-sensing materials [6-11] to implantable soft robotic devices [12, 13], to pneumatic actuators [14-18]. Inspired by biology, soft robots aim to actively and safely interact with their environment through high compliance [19-21]. Traditional, rigid-bodied robots are typically unsafe for human interaction and are designed to perform a single task efficiently, but often with limited adaptability. In contrast to rigid-bodied robots, soft robots have a continuously deformable structure,

allowing them to better absorb the energy from a collision [22]. Soft robots exhibit unprecedented adaptation and sensitivity, making them ideal for navigating through confined spaces. Cianchetti et al. present a single chamber soft robotic module for minimally invasive applications that produces 120º bending angle upon inflation [23]. The aim of this work is to explore various pneumatic actuator shapes to produce the maximum achievable bending angle with a single chamber module.

In this study, a modular, soft-robotic pneumatic actuator for potential applications in endoscopy was designed and fabricated. The soft robot was actuated with air pressure, making it suitable for use in MRI. The actuator was fabricated quickly and economically with a fused deposition modelling (FDM) 3D printer, greatly reducing manufacturing time and cost. The actuator design comprised of a curled resting position to achieve a greater bending angle upon actuation. It permitted only one degree of freedom, but the modular design allowed for multiple actuators to be connected in various configurations to achieve multiple degrees of freedom. The relationship between the actuator end effector displacement, inflation pressure, and external forces was modelled via a polynomial regression and a feedforward neural network. End effector displacement was measured via electromagnetic (EM) tracking, inflation pressure was measured via a pressure gauge, and external force was measured via manually applied loading. As this work was aimed at providing a proof of concept, practical safety concerns such as biocompatibility and sterilization were not evaluated. Future work will include biocompatibility design as well as modelling loading in various directions, distributed loading and torque.

Pneumatic Actuator Design

Modular Soft Robot Design

The soft robotic actuator was designed using SolidWorks and 3D printed using a Lulzbot Taz-6 printer. The Lulzbot Taz-6 is an FDM 3D printer and the printer filament is NinjaTek Ninjaflex, a thermoplastic polyurethane material. Various 3D printers and filaments were tested for comparison (Fig. 7.1), but ultimately Ninjaflex was chosen as the actuator material due to its superior flexibility. The advantage of high flexibility is that it allows for greater expansion of the fluidic chamber, resulting in a larger bending angle.

(a) Elongation at failure

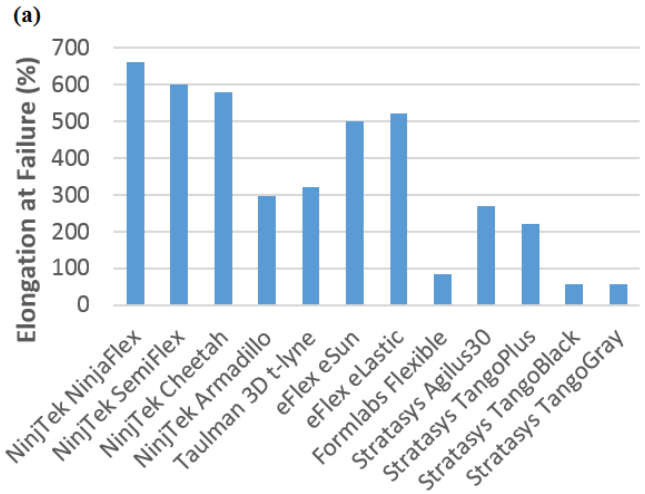

(b) Tensile strength

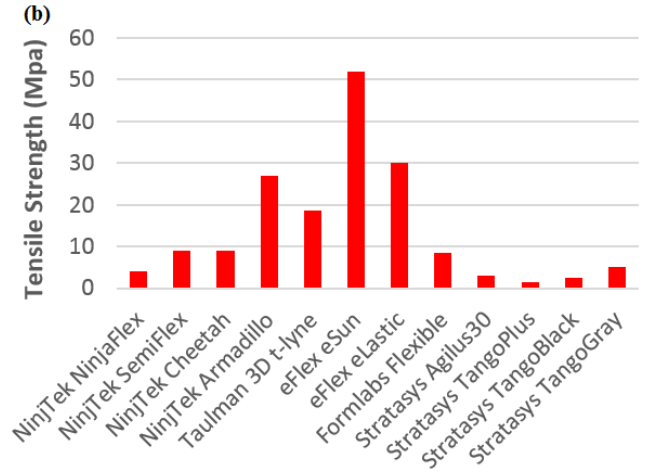

(c) Price per kg

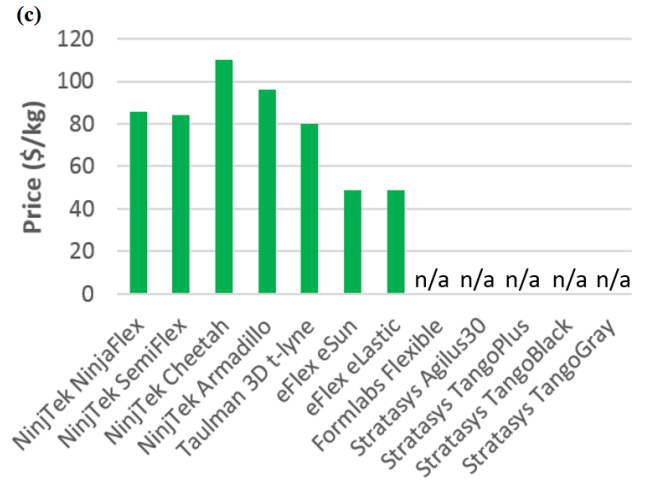

Figure 7.1. 3D printing filament specifications comparison.

A key consideration in the design of the actuator was the ability to provide a maximum bending angle upon inflation. Typical soft robots are designed with a straight-line resting (deflated) shape, aimed at achieving multiple degrees of freedom using multiple inflation chambers. With the goal of achieving a maximum bending angle, our actuator design sacrifices the ability to have multiple degrees of freedom and embodies a curled resting shape (Fig. 7.2a), which is achieved by 3D printing the actuator in the curled shape. The curled resting shape allows for a greater range of bending in a single direction by utilizing the advantage of already being bent 180º in the resting position.

The relevant dimensions of the actuator are presented in Table 7.1. The actuator was printed using a layer height of 0.4 mm, but the overall size of the actuator can be miniaturized by reducing the layer height. For simplicity and uniformity, the wall thickness was made constant throughout the entire actuator. The current dimensions of the actuator were not optimized for specific applications in minimally invasive surgery. The current work is a proof of concept aimed at evaluating the capabilities of the actuator for surgical applications. The optimization of the dimensions for a specific surgical procedure were outside the scope of this work.

Table 7.1. Dimensions of the Pneumatic Actuator

Deflated height, length, width	Inflated height, length, width	Wall thickness	Fluidic chamber volume	Air inlet diameter
45 x 30 x 10 mm	60 x 26.5 x 10 mm	0.8 mm	884 mm3	3.6 mm

Male and female connection components were incorporated into opposite ends of the actuator to enable a modular design. The fluidic chamber does not enter the joint components, making the joints unaffected by inflation. The design of the joint allows for

two actuators to be connected to each other in four different configurations, each offset by 90º rotation from each other, permitting the configuration to achieve multiple degrees of freedom. The joints were designed to connect to each other by creating a tight fitting between the male and female parts and can withstand a maximum tensile load of 14 N without disconnecting. The actuator contains a single air inlet (Fig. 7.2a). Fig. 7.2b shows a 3D printed actuator and Fig. 7.2c shows the cross-sectional view of the actuator as well as the direction of actuation. Figs. 7.2d, 7.2e, and 7.2f display various possible configurations for connecting multiple actuators.

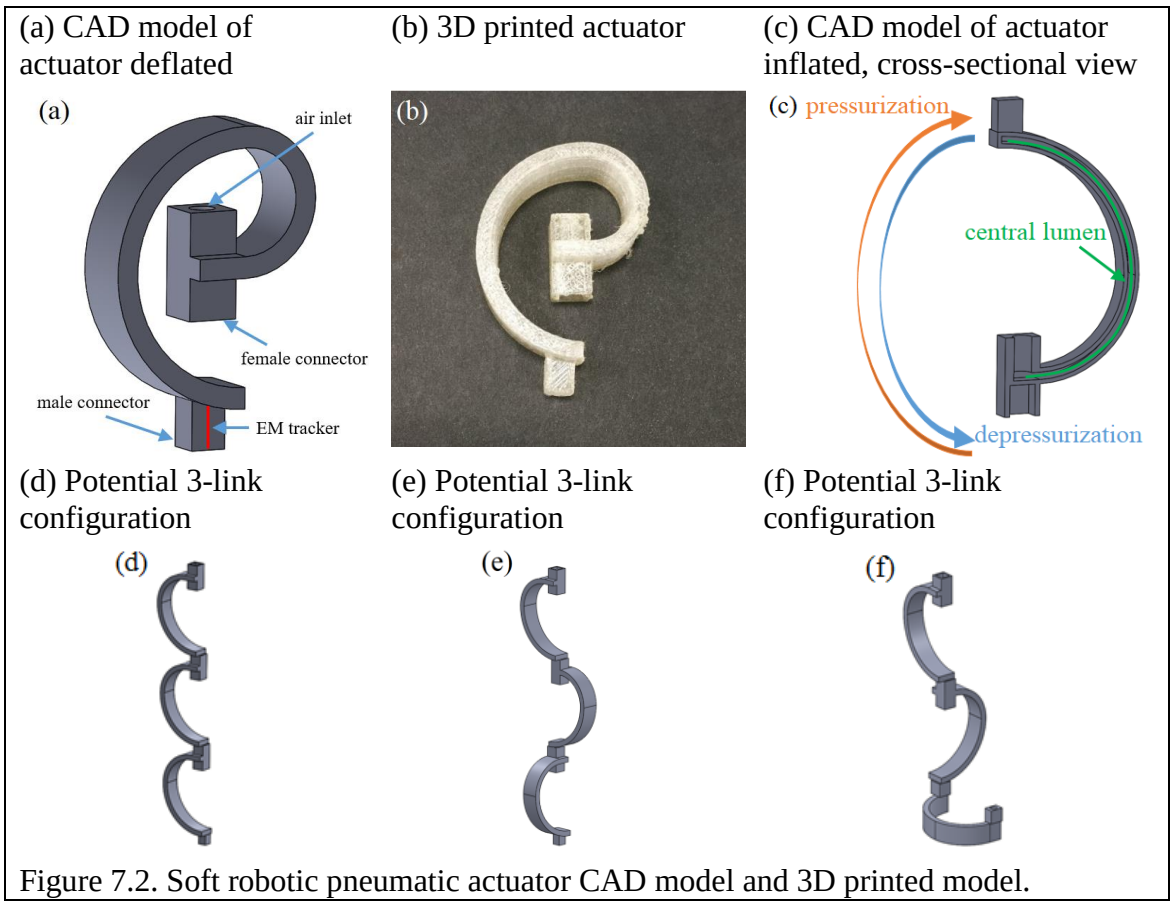

Figure 7.2. Soft robotic pneumatic actuator CAD model and 3D printed model.

Static Model of the Soft Robot with Image Processing

A MATLAB program was developed to model the curvature of the actuator based on processed images of the actuator under various gauge pressure levels so that the repeatability and maximum bending angle could be accurately measured. The actuator was held with a clamp upright (gravity loaded) at the base of the actuator during the experiment and images were taken with the actuator deflated and fully inflated (Figs. 7.3a & 7.3d). The images were processed in MATLAB with the edge detection feature to create a trace of the outline of the actuator (Figs. 7.3b & 7.3e). The inside arc of the trace was reconstructed by splitting the arc into six segments, estimating the curvature of each segment using the arc radius equation (1), and splicing the resulting segments together (Figs 7.3c & 7.3f). The arc radius equation is a manipulation of the intersecting chords theorem (Fig. 7.4). The intersecting chords theorem states that when two chords intersect each other inside a circle, the products of their segment lengths are equal (Fig. 7.5a). If one of the intersecting chords bisects the other chord, the intersecting chords theorem can be used to derive the arc radius equation (Fig. 7.5b).

(a) Deflated actuator photo

(b) Deflated actuator image processing

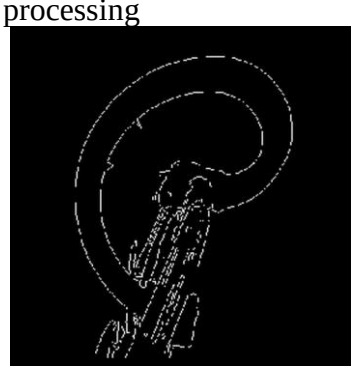

(c) Deflated actuator inner arc reconstruction

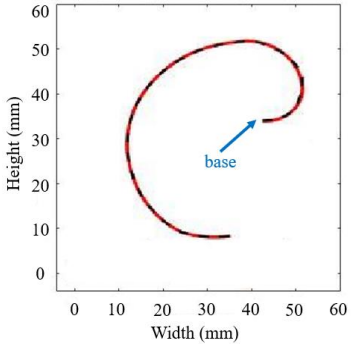

(d) Inflated actuator photo

(e) Inflated actuator image processing

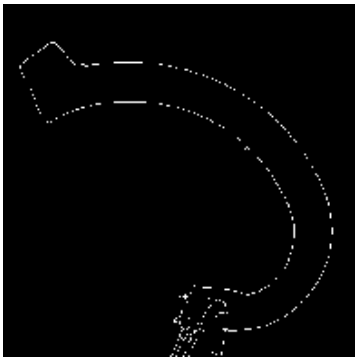

(f) Inflated actuator inner arc reconstruction

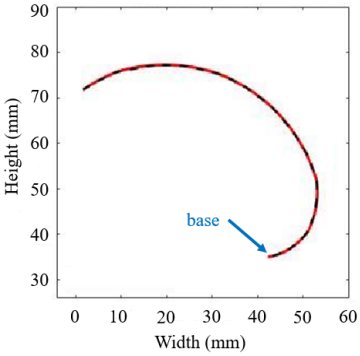

Figure 7.3. Experimental setup and image processing via MATLAB.

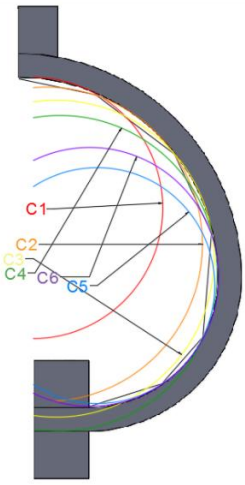

Figure 7.4. Inner curvature of soft robotic actuator approximated by dividing the arc into six segments and calculating the radius of each segment.

(a) Diagram showing the intersecting chords theorem

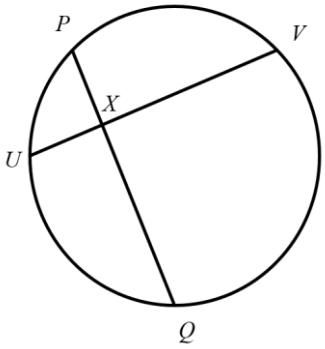

$$UX * XV = PX * XQ$$

(b) Diagram showing the derivation of the arc radius equation

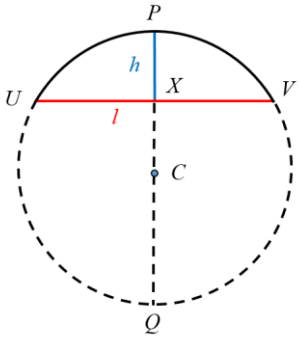

$$CQ = \frac{4XP^2 + UV^2}{8XP^2}$$

Figure 7.5. Geometrical analysis for deriving the arc radius equation.

The length of the chord, *l*, and the length of the segment between the center point of the arc to the midpoint of the chord, labeled *h*, are the only needed values to calculate the arc radius, *R*.

$$R = \frac{4h^2 + l^2}{8h} \tag{1}$$

A starting point (x_s, y_s), an endpoint (x_e, y_e), and a center point (x_c, y_c) were manually selected for each of the six segments s_n, totaling 18 (x, y) coordinate points for approximating the curvature.

$$s_n = \begin{bmatrix} x_s & y_s \\ x_e & y_e \\ x_c & y_c \end{bmatrix} \tag{2}$$

After developing a model for the curvature, the performance of the actuator was evaluated by measuring the repeatability and the maximum bending angle resulting from full inflation.

Electromagnetic tracking-based force approximation

The actuator was placed under various tensile loading and gauge pressures to understand and predict the end effector displacement behavior. To quickly and accurately

track the displacement of the end effector upon loading, the actuator was equipped with a Northern Digital Inc. (NDI) five degree-of-freedom EM tracking sensor. An Aurora V3 Planar Field Generator was used to generate a magnetic field to track the sensor. The EM sensor was mounted to the end effector of the actuator and connected to the Aurora Sensor Interface Unit and System Control Unit. EM tracking was conducted in a 500 mm × 500 mm × 500 mm working volume located 50 mm away from the front of the Aurora field generator (Fig. 7.6). The actuator was mounted at the air inlet location as shown in Fig. 7.3a, allowing the opposite end to move freely. A uniaxial tensile load was applied vertically downward by hanging weights from the end effector of the actuator. The actuator displacement was measured at various gauge pressures ranging from 10 to 35 psi in increments of 5 psi, and at various loads ranging from 0 to 120 grams in increments of 10 grams. All displacements reported are maximum displacement. The time taken to achieve maximum displacement was also measured and reported.

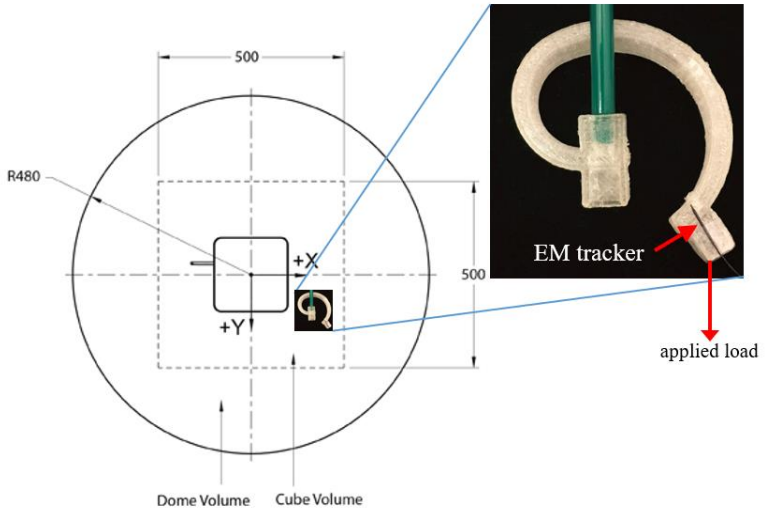

Figure 7.6. Diagram depicting the actuator in Aurora magnetic field [24]. Values are expressed in millimeters. The red arrows indicate the location of the EM tracker and the direction of the applied load.

Feedforward Neural Network

The EM tracking displacement data was fed into a single layer feedforward neural network in MATLAB. Three sets of the displacement data were collected at each combination of gauge pressure and tensile loading for a total of 234 data points. A randomly selected 70% of the data was used to train the neural network, 15% of the data was used as a validation set, and 15% was used as a test set. The network architecture consists of two inputs (inflation pressure, load), a single hidden layer with four units, and an output layer with a single linear activation (displacement). The network was trained using the Levenberg-Marquardt algorithm until the validation error stopped improving, thus preventing overfitting.

Pneumatic Actuator Evaluation

Actuator Performance Evaluation

The performance of the actuator was evaluated by measuring the repeatability and the maximum bending angle. The end effector displacement (mm) was measured at 5 psi intervals ranging from 10 to 35 psi using the arc radius curvature model. The repeatability was evaluated by computing the mean error of the end effector displacement of three different trials at each pressure level for a single actuator (Fig. 7.7). The results show an error of less than 1.2 mm at each of the six different pressure levels, demonstrating that the actuator can be accurately controlled by regulating the gauge pressure. The maximum bending angle achieved for a single actuator was 145º with an applied gauge pressure of 35 psi. This is a greater maximum bending angle than most other pneumatic actuators in the literature, without the need for a crimped external shell [23] or fiber reinforcement [18].

(a) 10 psi

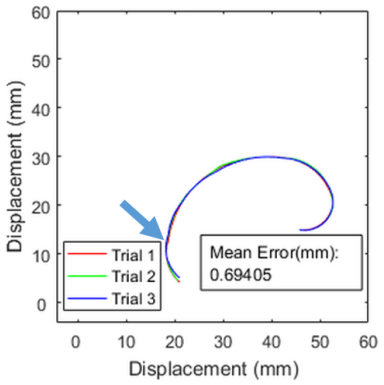

(b) 15 psi

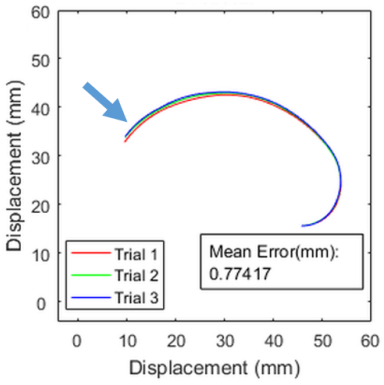

(c) 20 psi

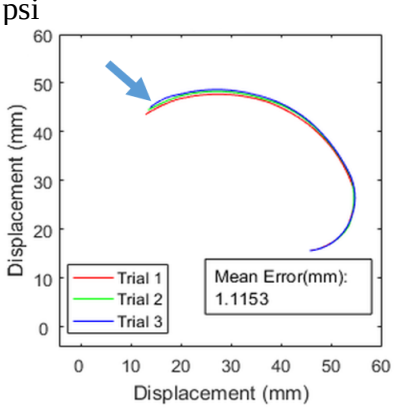

(d) 25 psi

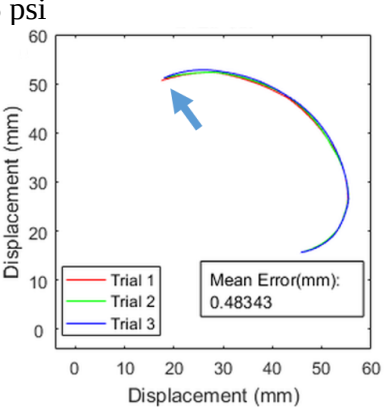

(e) 30 psi

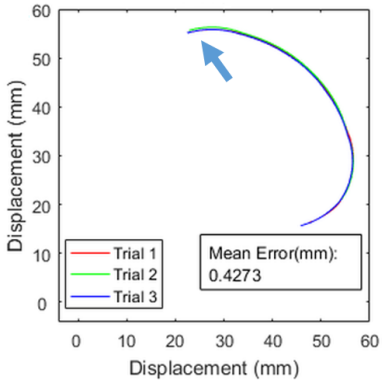

(f) 35 psi

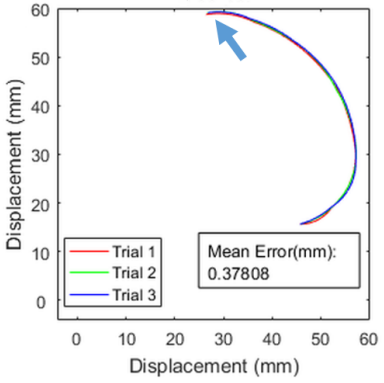

Figure 7.7. Plot showing the repeatability of the tip displacement upon inflation. Blue arrows show the position of the actuator tip under gauge pressure levels from 10-35 psi.

EM Tracking Repeatability Analysis

The repeatability of the EM tracker was determined by computing the mean error of the end effector displacement (mm) of ten different trials at each gauge pressure level for a single actuator. Fig. 7.8 displays the mean displacement error of the ten different trials for each gauge pressure level, with error bars displaying the standard deviation. The maximum mean displacement error was approximately 0.47 mm with a standard deviation of less than 0.1 mm, validating the repeatability of the EM tracking method.

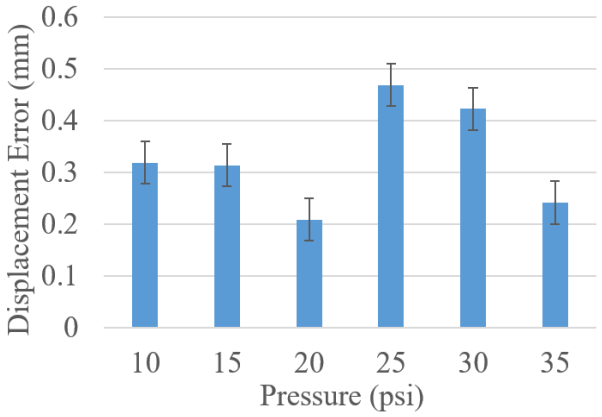

Figure 7.8. Mean displacement error of ten trials for each gauge pressure level with error bars displaying the standard deviation.

Polynomial Regression Model

The ability of the soft robotic actuator to withstand tensile loading was modeled using a fourth-order polynomial regression model. The regression model is presented in Fig. 7.9 and the parameter values are listed in Table 7.2. The model shows a significant change in the behavior and overall displacement in the actuator when the applied load is greater than 50 g (0.5 N). The model yielded an average coefficient of correlation value, R, of 0.99834. The time taken to achieve maximum displacement for each of the reported measurements was on average 0.4 seconds.

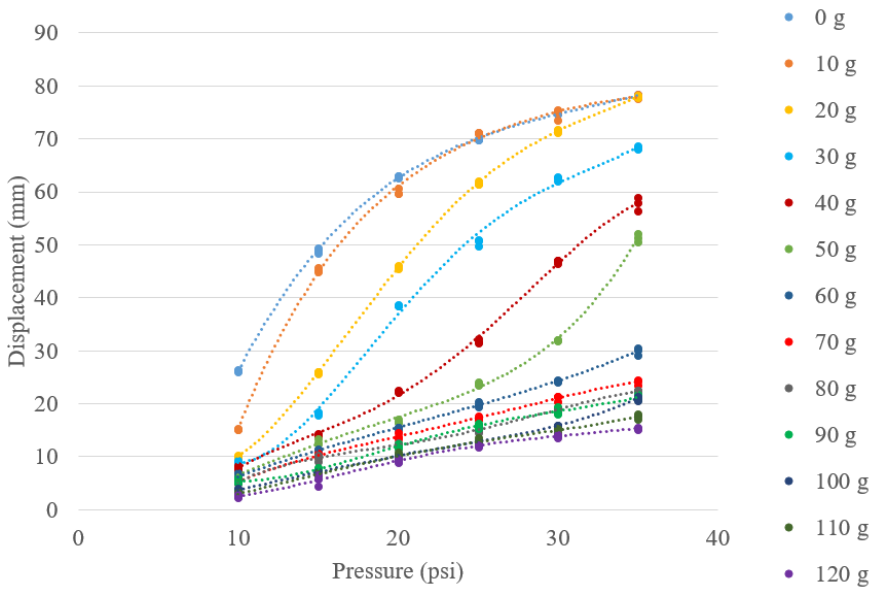

Figure 7.9. Fourth-order polynomial regression of pressure vs displacement as the load varies from 0 - 120 g (0 - 1.18 N).

Table 7.2. Fourth-Order Polynomial Regression Model Parameter Values

Weight(g)	β0	β1	β2	β3	β4
0	-65.571	13.275	-0.4855	0.0081	-0.00005
10	-116.26	20.082	-0.853	0.0174	-0.0001
20	47.904	-12.38	1.1772	-0.0353	0.0004
30	85.079	-19.113	1.5518	-0.0448	0.0004
40	-41.872	10.161	-0.7504	0.0261	-0.0003
50	-2.8065	0.0911	0.1498	-0.008	0.0001
60	-7.519	1.7332	-0.0418	0.0006	0.00006
70	-18.532	4.0303	-0.2221	0.0064	-0.00007
80	-30.602	6.7933	-0.4358	0.0129	-0.0001
90	25.857	-4.9997	0.399	-0.01115	0.0001
100	0.9713	-0.4197	0.1071	-0.0044	0.00006
110	-0.7429	-0.2418	0.0914	-0.0034	0.00004
120	7.8102	-1.991	0.202	-0.0063	0.00007

Feedforward Neural Network

The performance of the neural network was measured by evaluating the mean squared error (MSE) between the output displacement values and the target displacement values. The model obtained an MSE of 1.2788 mm on the validation set at the 22nd epoch (Fig. 7.10). The coefficient of correlation value, R, was 0.99639 for the training set, 0.99471 for the validation set, 0.99737 for the test set, and 0.99643 overall (Fig. 7.11). In comparison to the polynomial regression model, the neural network performed worse by 0.2%. Although the neural network performed slightly worse than the polynomial regression, it is a robust computer-assisted method for controlling the actuator that can easily scale with larger datasets and additional features.

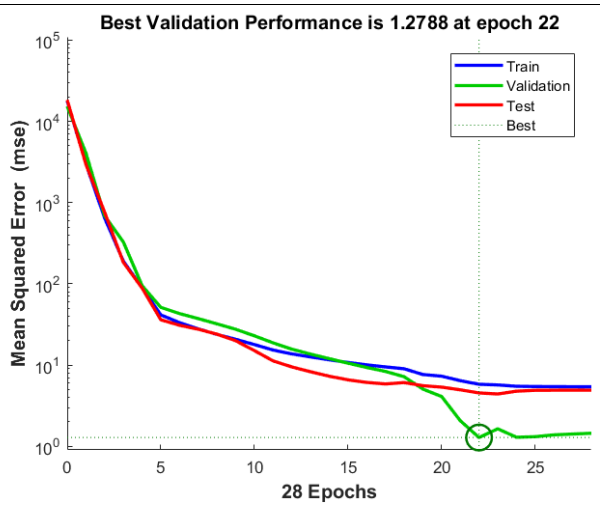

Figure 7.10. Neural network performance evaluation.

(a) Training set

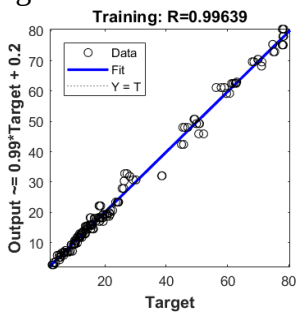

(b) Validation set

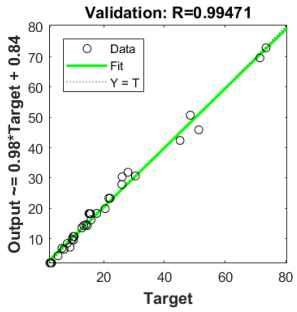

(c) Test set

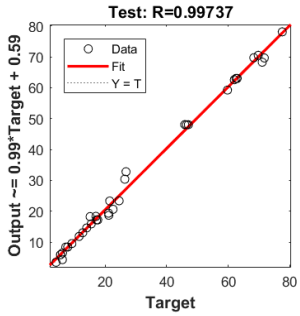

(d) Training, validation and test data combined

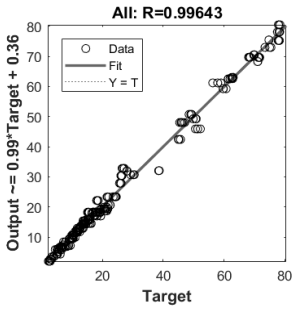

Figure 7.11. Neural network regression analysis.

Discussion

This chapter presented the development of a modular pneumatic soft robotic actuator that can be used to form a multi-degree-of-freedom steerable mechanism for potential applications in MIS. The proposed actuator was 3D printed in under one hour and costs less than one US dollar. The curled design of the actuator achieved a greater maximum bending angle upon actuation than other pneumatic actuators reported in the literature. The intersecting chords theorem was applied to develop a mathematical model of the actuator that was used to measure the bending performance and the repeatability. An EM tracker is attached to the distal end of the actuator and used to track the end effector position as various loads are applied. A fourth-order polynomial regression model to show the relationship between the load, the inflation pressure, and the end

effector displacement was developed. Finally, a feedforward neural network model to control the actuator was developed.

The modular soft robotic actuator presented in this work is an extremely low-cost approach for constructing complex multi-degree-of-freedom soft robotic systems. As this work is aimed at providing a proof of concept, practical safety concerns such as biocompatibility and sterilization were not evaluated. Future work will include biocompatibility design as well as modeling multiaxial loading, distributed loading and torque.

References

[1] S. F. Elahi and T. D. Wang, "Future and advances in endoscopy," Journal of biophotonics, vol. 4, no. 7-8, pp. 471-481, 2011.

[2] E. J. Seibel, R. S. Johnston, and C. D. Melville, "A full-color scanning fiber endoscope," in Optical Fibers and Sensors for Medical Diagnostics and Treatment Applications VI, 2006, vol. 6083, p. 608303: International Society for Optics and Photonics.

[3] J. E. Moore Jr and D. J. Maitland, Biomedical technology and devices. CRC press, 2013.

[4] C. M. Lee, C. J. Engelbrecht, T. D. Soper, F. Helmchen, and E. J. Seibel, "Scanning fiber endoscopy with highly flexible, 1 mm catheterscopes for wide-field, full-color imaging," Journal of biophotonics, vol. 3, no. 5-6, pp. 385-407, 2010.

[5] E. Lippert, H. H. Herfarth, N. Grunert, E. Endlicher, and F. Klebl, "Gastrointestinal endoscopy in patients aged 75 years and older: risks,

complications, and findings—a retrospective study," International journal of colorectal disease, vol. 30, no. 3, pp. 363-366, 2015.

[6] N. Lu and D.-H. Kim, "Flexible and stretchable electronics paving the way for soft robotics," Soft Robotics, vol. 1, no. 1, pp. 53-62, 2014.

[7] T. Q. Trung and N. E. Lee, "Flexible and Stretchable Physical Sensor Integrated Platforms for Wearable Human-Activity Monitoringand Personal Healthcare," Advanced materials, vol. 28, no. 22, pp. 4338-4372, 2016.

[8] Y. Gao, H. Ota, E. W. Schaler, K. Chen, A. Zhao, W. Gao, H. M. Fahad, Y. Leng, A. Zheng, and F. Xiong, "Wearable Microfluidic Diaphragm Pressure Sensor for Health and Tactile Touch Monitoring," Advanced Materials, vol. 29, no. 39, 2017.

[9] K. B. Shimoga and A. A. Goldenberg, "Soft materials for robotic fingers," in Robotics and Automation, 1992. Proceedings., 1992 IEEE International Conference on, 1992, pp. 1300-1305: IEEE.

[10] R. S. Dahiya, G. Metta, M. Valle, and G. Sandini, "Tactile sensing—from humans to humanoids," IEEE transactions on robotics, vol. 26, no. 1, pp. 1-20, 2010.

[11] P. Polygerinos, Z. Wang, K. C. Galloway, R. J. Wood, and C. J. Walsh, "Soft robotic glove for combined assistance and at-home rehabilitation," Robotics and Autonomous Systems, vol. 73, pp. 135-143, 2015.

[12] C. J. Payne, I. Wamala, C. Abah, T. Thalhofer, M. Saeed, D. Bautista-Salinas, M. A. Horvath, N. V. Vasilyev, E. T. Roche, and F. A. Pigula, "An implantable extracardiac soft robotic device for the failing heart: Mechanical coupling and synchronization," Soft robotics, vol. 4, no. 3, pp. 241-250, 2017.

[13] D. Van Story, M. Saeed, K. Price, I. Wamala, P. E. Hammer, D. Bautista-Salinas, D. M. Vogt, C. J. Walsh, R. J. Wood, and N. V. Vasilyev, "Approaches to Real-Time Ventricular Wall Strain Measurement for the Control of Soft Robotic Ventricular Assist Devices."

[14] T. Noritsugu, H. Yamamoto, D. Sasakil, and M. Takaiwa, "Wearable power assist device for hand grasping using pneumatic artificial rubber muscle," in SICE 2004 Annual Conference, 2004, vol. 1, pp. 420-425: IEEE.

[15] T. Noritsugu, "Pneumatic soft actuator for human assist technology," in Symposium on Fluid Power, 2005, vol. 2005.

[16] L. Connelly, Y. Jia, M. L. Toro, M. E. Stoykov, R. V. Kenyon, and D. G. Kamper, "A pneumatic glove and immersive virtual reality environment for hand rehabilitative training after stroke," IEEE Transactions on Neural Systems and Rehabilitation Engineering, vol. 18, no. 5, pp. 551-559, 2010.

[17] G. K. Klute, J. M. Czerniecki, and B. Hannaford, "McKibben artificial muscles: pneumatic actuators with biomechanical intelligence," in Advanced Intelligent Mechatronics, 1999. Proceedings. 1999 IEEE/ASME International Conference on, 1999, pp. 221-226: IEEE.

[18] J. Bishop-Moser, G. Krishnan, C. Kim, and S. Kota, "Design of soft robotic actuators using fluid-filled fiber-reinforced elastomeric enclosures in parallel combinations," in Intelligent Robots and Systems (IROS), 2012 IEEE/RSJ International Conference on, 2012, pp. 4264-4269: IEEE.

[19] S. Kim, C. Laschi, and B. Trimmer, "Soft robotics: a bioinspired evolution in robotics," Trends in biotechnology, vol. 31, no. 5, pp. 287-294, 2013.

[20] B. A. Trimmer, H.-T. Lin, A. Baryshyan, G. G. Leisk, and D. L. Kaplan, "Towards a biomorphic soft robot: design constraints and solutions," in Biomedical Robotics and Biomechatronics (BioRob), 2012 4th IEEE RAS & EMBS International Conference on, 2012, pp. 599-605: IEEE.

[21] R. Pfeifer, M. Lungarella, and F. Iida, "The challenges ahead for bio-inspired'soft'robotics," Communications of the ACM, vol. 55, no. 11, pp. 76-87, 2012.

[22] D. Rus and M. T. Tolley, "Design, fabrication and control of soft robots," Nature, vol. 521, no. 7553, p. 467, 2015.

CHAPTER 8

CONCLUSIONS AND FUTURE WORK

Aims of this Dissertation

The aim of this dissertation is to present the development of non-rigid diagnostic and interventional medical devices for image-guided minimally invasive procedures. A further objective is demonstrating the development of these devices using rapid prototyping techniques. This innovative fabrication process provides quick and low-cost manufacturing that allows for the devices to be disposable, which is ideal in the surgical environment as there is no required hassle of sterilization after use. In addition, rapid prototyping fabrication also allows for customization of the product to suit the anatomy of a specific patient or the course of a specific procedure. The work presented in this dissertation provides insight for what the future holds in minimally invasive procedures with continual technological advances in 3D printing and other rapid prototyping technologies.

Outlook and Future Work

The continuation of the body of work presented in this dissertation lies within the further development of three specific areas of focus: (1) rapid prototyping of contrast agent markers for image-guided interventions (Ch: 2-3); (2) the use of origami in designing unique devices which can store medical instruments to be inserted into the body and deploy the instruments once inside the anatomy of interest (Ch. 5); and (3) the

development of novel disposable endoscopes for image-guided minimally invasive procedures (Ch. 6-7).

1) Rapid Prototyping of Contrast Agent Markers

Based on the developments in creating a custom radiocontrast agent mixture, designing a method for printing the custom mixture, and manipulating various printed patterns, the potential for growth in the field of contrast agent markers is increased. The work presented in this dissertation focused on the use of the radiocontrast agent barium sulfate. There are various other radiocontrast agents commonly used in CT such as iodine-based solutions to be explored. Additionally, contrast agents for use within MRI such as gadolinium-based solutions have the potential for use in custom markers. The ability to create custom 2D and 3D markers opens the door to a wide range of potential structures which might be used in various situations and procedures.

2) Deployable Origami Devices

An origami structure which folds from a wide and flat surface into a compact three-dimensional shape was presented in this dissertation, storing an MRI receiver coil at the distal end of a catheter for deploying inside the human body. Further development of this methodology would allow for safe and reliable techniques for deploying and restowing the structure, either through the incorporation of mechanical actuators or the use of a self-folding material. The utilization of origami techniques in the design of medical devices offers enormous potential for significant advances due to the ability to change shape inside the body, an environment that imposes challenging space constraints.

3) Disposable Endoscopes

Preliminary designs have been presented regarding MR conditional modular actuators which have the potential for use as endoscopic devices. This has resulted in the development of devices that can be controlled to move in specific directions within the MRI environment without posing dangerous effects or degrading image quality. In order to translate this technique into the clinic, further research must be conducted towards miniaturizing the devices to a size suitable for inserting into the human body. Additionally, more advanced control systems for controlling multiple actuators at a time must be derived and implemented. Upon miniaturization and reliable control of a chain of actuators, the potential for this technology to be integrated into the MRI environment will grow, allowing for the use of low-cost, disposable endoscopes for minimally invasive procedures.

CHAPTER 9

PUBLICATIONS

Current

Journal Articles

[1] **A. J. Taylor**, Y. Chen, M. Fok, A. Berman, K. Nilsson, Z. T. H. Tse, "Cardiovascular Catheter with an Expandable Origami Structure," *Journal of Medical Devices*, 2016.

[2] **A. J. Taylor**, J. Dai, A. Squires, P. Shen, Z. T. H. Tse, "Pneumatic Transport System for Associative Learning in Larval Drosophila Melanogaster," *Advanced Techniques in Biology and Medicine*, 2018.

[3] **A. J. Taylor**, R. Montayre, Z. Zhao, Ka Wai Kwok, Z. T. H. Tse, "Modular Force Approximating Soft Robotic Pneumatic Actuator," *International Journal of Computer Assisted Surgery*, 2018.

[4] **A. J. Taylor**, T. Slutzky, L. Feuerman, Z. T. H. Tse, "MR Conditional Flexible Endoscopic Design Based on Origami," *IEEE Transactions on Mechatronics*, 2019.

[5] **A. J. Taylor**, S. Xu, B. J. Wood, Z. T. H. Tse, "Origami Lesion-Targeting Device for CT-Guided Interventions," *Journal of Imaging*, 2019.

2) Conference Abstracts

[1] **A. J. Taylor**, M. Miller, M. Fok, K. Nilsson, Z. T. H. Tse, "Intracardiac Magnetic Resonance Imaging Catheter with Origami Deployable Mechanisms," *Design of Medical Devices*, Minneapolis, MN, vol. 10, 2016.

[2] **A. J. Taylor**, Y. Chen, E. Schmidt, Z. T. H. Tse, "Applying Origami Coil Design for Deployable Intra-cardiac MRI Catheter," *23rd Annual Meeting of the International Society for Magnetic Resonance in Medicine*, Singapore, 2016.

[3] **A. J. Taylor**, Y. Chen, E. Schmidt, Z. T. H. Tse, "Intra-cardiac Magnetic Resonance Imaging Catheter with Origami Deployable Structure," *8th National Center for Image Guided Therapy Workshop*, Bethesda, MD, 2016.

[4] **A. J. Taylor**, T. Slutzky, L. Feuerman, M. Fok, Z. T. H. Tse, "Origami Endoscope Design for MRI-Guided Therapy," *Design of Medical Devices Conference*, Minneapolis, MN 2017

[5] **A. J. Taylor**, M. Nuriyev, R. Montayre, Z. T. H. Tse, "Soft-Robotic Endoscope Tip Design," Design of Medical Devices Conference, Minneapolis, MN, 2017

[6] **A. J. Taylor**, R. Montayre, Z. Zhao, Z. T. H. Tse, "Modular Force Sensing Soft Robotic Pneumatic Actuator," *International Symposium on Medical Robotics*, Atlanta GA, 2018

[7] **A. J. Taylor**, T. Pham, Z. Zhao, R. Montayre, S. Xu, B. Wood, Z. T. H. Tse, "CT-guided Abdominal Biopsy Training Phantom," *International Symposium on Medical Robotics*, Atlanta GA, 2018.

[8] **A. J. Taylor**, S. Xu, B. J. Wood, Z. T. H. Tse, "Rapid Prototyping of Patient Specific CT Markers," *International Symposium on Medical Robotics*, Atlanta GA, 2019.

Under Review

1) Journal Articles

[1] **A. J. Taylor**, S. Xu, B. J. Wood, Z. T. H. Tse, "Rapid Prototyping of Custom Radiocontrast Agent Markers for CT- Guided Procedures," *Annals of Biomedical Engineering*, Under Review, 2019.